

The Hyper Suprime-Cam extended Point Spread Functions and applications to measuring the intra-halo light

Lucía P. Garate-Nuñez,^{1,2*} Aaron S. G. Robotham,^{1,2} Sabine Bellstedt,¹ Luke J. M. Davies,¹ Cristina Martínez-Lombilla^{2,3,4}

¹ICRAR, The University of Western Australia, 35 Stirling Highway, Crawley, WA 6009, Australia

²Australian Research Council Centre of Excellence for All-Sky Astrophysics in 3 Dimensions (ASTRO 3D), Stromlo, ACT 2611, Australia

³School of Physics and Astronomy, Monash University, Clayton, Victoria 3800, Australia

⁴School of Physics, University of New South Wales, Sydney, NSW 2052, Australia

Accepted XXX. Received YYY; in original form ZZZ

ABSTRACT

We present extended point spread function (PSF) models for the Hyper Suprime-Cam Subaru Strategic Program Public Data Release 3 (HSC-SSP PDR3) in all g, r, i, Z and Y -bands. Due to its 8.2m primary mirror and long exposure periods, HSC combines deep images with wide-field coverage, making it one of the most suitable observing facilities for low surface brightness (LSB) studies. By applying a median stacking technique of point sources with different brightnesses, we show how to construct the HSC-SSP PDR3 PSF models to an extent of $R \sim 5.6$ arcmin. These new PSFs provide the community with a crucial tool to characterise LSB properties at large angles. We apply our HSC PSFs and demonstrate that they behave reasonably in two cases: first, to generate a 2-D model of a bright star, and second, to remove the PSF-scattered light from an Ultra Deep image of the 400020 Galaxy And Mass Assembly (GAMA) group in the SXDS field. Our main focus in this second application is characterising the r -band intra-halo light (IHL) component of 400020. Building on advanced source extraction techniques with careful consideration of PSF flux, we measure the IHL surface brightness (SB) group profile up to ~ 31 mag arcsec $^{-2}$ and $R = 300$ kpc. We estimate the IHL fraction (f_{IHL}) profile, with a mean of $f_{\text{IHL}} \sim 0.13$. Our results show that not removing the PSF light can overestimate the IHL SB by ~ 1.7 mag arcsec $^{-2}$ and the f_{IHL} by $\sim 30\%$.

Key words: instrumentation: detectors – galaxies: clusters: intracluster medium – galaxies: haloes – methods: data analysis – techniques: image processing – techniques: photometric

1 INTRODUCTION

Atmospheric conditions and the optics of each of the telescope, instruments, and detectors are the two main reasons why the light of a point source is spread in astronomical images. To quantify this scatter, scientists have defined a function known as point spread function (PSF, Born & Wolf 1999). The PSF describes the two-dimensional light distribution in the telescope focal plane produced by point sources, where extensive studies have been performed to carefully characterise the imaging system.

The inner part of the PSF (within a few tens of arcseconds) is dominated by atmospheric turbulence (Kolmogorov 1941) and is generally well represented by a Moffat function (Moffat 1969; Racine 1996). An accurate determination of the inner part of the PSF is necessary to recover the real information of the point source and remove the light that is contaminating the surroundings of the bright stars. In the case of studying low surface brightness (LSB) galaxies and features, we also need an accurate determination of the extended PSF profile to remove its faint scattered light that contaminates at large distances from the point source. The outer region of the PSF is

less understood and was first measured by King 1971, who attributes an r^{-2} behaviour to this part of the radial profile (de Vaucouleurs 1958). Subsequent measurements mostly fitted the PSF wings with a power-law profile, where the power index ranges from 1.6 to 3 (Gonzalez et al. 2005; Bernstein 2007; Slater et al. 2009). In addition, the PSF spreads the light from all sources (not only point sources Sandin 2014; Trujillo & Fliri 2016; Tang et al. 2018). Because of this, the PSF modeling will play a crucial role in two different steps: recovering the spread light from point and extended sources and also removing this contaminating light from the image.

Although the PSF becomes rapidly fainter with increasing r , the total integrated light from the outer region could have an effect when estimating LSB sources (Gallagher & Ostriker 1972; Merritt 1984; Uson et al. 1991; Murante et al. 2004; Mihos et al. 2005; Martínez-Lombilla & Knapen 2019; Montes 2022). de Vaucouleurs 1948, 1953, 1958 focused on how scattered light affects large elliptical galaxies observations, where the effects of the PSF were found to be of minor importance. However, more recent works have found that the measured amount of stellar light in the halos could be affected by the PSF.

Star images can be combined to extract the principal components of the PSF signature via the stacking method (La Barbera et al. 2012;

* E-mail: lucia.garatenunez@research.uwa.edu.au

D’Souza et al. 2014). For example, de Jong 2008 worked with data in the Hubble Ultra Deep Field (HUDF; Beckwith et al. 2006) of the Hubble Space Telescope (HST) and stacked Sloan Digital Sky Survey (SDSS; York et al. 2000) images to estimate the effect of the PSF wings on edge-on galaxies, finding a significant impact on the measured stellar halos. Trujillo & Bakos 2013 used the TinyTim HST PSF modeling software (Krist 1995) to generate the Hubble UDF PSF and conclude that scattered light from the extended PSF has a major impact on the surface brightness galaxy profiles.

Telescopes that are highly optimized for low surface brightness have a true PSF that is well behaved and easy to model. The absence of reflective surfaces, anti-reflection coatings, an unobstructed pupil, and a fast focal ratio are the main characteristics of a telescope suitable for studying LSB sources (Abraham & van Dokkum 2014). Slater et al. 2009 made an effort to mitigate the multiple internal reflections of bright point sources that complicate the estimation of the extended stellar PSF on the Case Western Reserve University’s Burrell Schmidt telescope located at the Kitt Peak National Observatory. These improvements helped to remove the excess light from extremely faint structures of the intracluster light around the Virgo cluster (Mihos et al. 2009; Janowiecki et al. 2010; Rudick et al. 2010). In the case of the Dragonfly Telephoto Array (Abraham & van Dokkum 2014), due to its wide field of view and optical coatings designed to minimize reflections, the array is suitable for studying extended stellar halos of luminous nearby galaxies (Merritt et al. 2016a,b; Cohen et al. 2018). Since it is composed of telephoto lenses, the Dragonfly Telephoto Array is likely to have more stable PSF wings than reflecting telescopes, as the latter introduces more scatter (Nelson et al. 2008). Merritt et al. 2020 indicate that the PSF effects are minimal at the Dragonfly galaxy outskirts. However, more stellar halo measurements are needed in order to analyse the effect of PSF wings.

Another competitive instrument for detecting low surface brightness emission is the Hyper Suprime-Cam (HSC; Miyazaki et al. 2015, 2018; Komiya et al. 2018; Kawanomoto et al. 2018). Attached at the prime focus of the Subaru Telescope (Mauna Kea, Hawaii) and developed by the National Astronomical Observatory of Japan, HSC is one of the state-of-the-art cameras that provides a wide field of view and is also capable of reaching deep optical imaging in a short exposure time. The HSC team developed the Hyper Suprime-Cam Subaru Strategic Program (HSC-SSP; Aihara et al. 2018), a survey with a coverage of 1400 deg^2 in five different bands ($griZY$) as well as four narrow filters. HSC-SSP is providing an unprecedented database for LSB studies. For example, Greco et al. 2018a detected ~ 800 low-surface brightness galaxies in the first 200 deg^2 of the Wide HSC-SSP layer, where approximately half of which are ultra-LSB with central surface brightnesses in the g -band of $\mu_0 > 24 \text{ mag arcsec}^{-2}$ (Greco et al. 2018b; Kado-Fong et al. 2021). Furnell et al. 2021 studied the intra-cluster light (ICL) growth using a sample of 18 X-Ray clusters with deep HSC data in the i -band between $0.1 < z < 0.5$. Given its coverage, depth, and image quality (median seeing in all bands of $\sim 0.7 \text{ arcsec}$), this survey can be seen as a predecessor of the upcoming Vera C. Rubin Observatory Legacy Survey of Space and Time (LSST; LSST Science Collaboration et al. 2009).

The HSC image processing pipeline (Bosch et al. 2018, 2019) estimates the PSF using a restructured version of the public PSFEx code (Bertin 2013). The approach of this code is to use unresolved star data in the field to estimate the PSF from an exposure, where the PSF model can be reconstructed for any location on the image. However, Mandelbaum & Hyper Suprime-Cam (HSC) Collaboration 2017 found that the PSFEx model of HSC PSF has super-resolution problems beyond a certain seeing threshold.

Montes et al. 2021 constructed an HSC PSF with g and i observations from HSC-SSP to analyse the intracluster light of the Abell 85 cluster of galaxies. The authors followed the method outlined by Infante-Sainz et al. (2020), which was originally designed for SDSS. In this method, the PSF reconstruction process is divided into three parts, using stars within a wide brightness range to build each region. Montes et al. 2021 used four parts instead, where the two inner parts are made by stacking stars of faint magnitude and the two outer parts are made by fitting a power-law function to the brightest star profile in the field and extrapolating it up to $R \sim 7 \text{ arcmin}$. Two years later, Martínez-Lombilla et al. 2023 followed the same method to characterise the HSC PSF with observations from the HSC-SSP Public Data Release 2 (Aihara et al. 2019). In this case, the authors divided the PSF into three parts and applied a median stacking technique of stars in each part for the g, r, i -bands up to an extent of $R \sim 5.6 \text{ arcmin}$ in the g and r -bands and $R \sim 4.2 \text{ arcmin}$ in the i -band. They used these PSF models to analyse the intra-halo light (IHL, also known as intra-group light or intra-cluster light) present in an intermediate-redshift Galaxy And Mass Assembly (GAMA, Driver et al. 2011) group of galaxies.

HSC-SSP PDR3 (Aihara et al. 2022) is the newest public data release from HSC, which is publicly accessible since August 2021. In comparison to both previous PDRs, this release increases the sky coverage to the required depths across all five filters. From PDR2 to PDR3, the partially observed area increased from 1114 deg^2 to 1470 deg^2 , where the covered area at full depth ($\sim 26 \text{ mag at } 5\sigma$) increased from 305 deg^2 to 670 deg^2 . In addition, due to a new global sky subtraction algorithm, the overall quality of the PDR3 data has also improved and the extended wings of bright sources are better preserved. By building on advanced source extraction techniques and following the method from Infante-Sainz et al. (2020), we characterise the HSC-SSP PDR3 PSFs in each of the g, r, i, Z and Y bands down to a radius of $R \sim 5.6 \text{ arcmin}$. The PSF image FITS files and the scripts to follow the PSFs reconstruction are made available to the astronomical community. We also used the PSFs to make an estimation of the fraction of IHL present in the 400020 GAMA group at redshift 0.258.

The structure of the paper is as follows. In Section 2 we discuss the data products used for this work. Section 3 explains the steps we follow to reconstruct the HSC-SSP PDR3 PSFs. We investigate and compare our methodology to derive the PSFs with other methodologies commonly used in the literature in Section 4. Section 5 is dedicated to testing the performance of the HSC-SSP PDR3 PSFs on two real observations. We first use the PSFs to generate 2D models of an HSC-SSP PDR3 bright star in Section 5.1. Secondly, in Section 5.2, we use the PSFs to analyse the IHL component in an Ultra Deep (UD) image of a GAMA group of galaxies. We summarise the results of this work in Section 6.

We adopt throughout an $H_0 = 68.4 \text{ km s}^{-1} \text{ Mpc}^{-1}$, $\Omega_\Lambda = 0.699$ and $\Omega_m = 0.301$ cosmological model, corresponding to the cosmology of Planck Collaboration et al. 2020. All magnitudes are in the AB magnitude system and the HSC-SSP PDR3 zero point magnitude is $m_{zero} = 27 \text{ mag}$.

2 DATA

In this work, we use data from the Hyper Suprime-Cam Subaru Strategic Program (Aihara et al. 2018). In particular, the images are from the last public data release of the HSC-SSP Survey, HSC-SSP PDR3 (Aihara et al. 2022). We use the Gaia Data Release 3 catalogue (Gaia Collaboration et al. 2022) to find the positions of the stars

that are used to obtain the empirical PSF models. The motivation to construct extended and well characterised HSC-SSP PDR3 PSFs is to improve our future research on studying the intra-halo light (IHL) that is present in groups and clusters of galaxies with HSC observations. Following this idea, we also use the GAMA galaxy group catalogue G³Cv10 (Robotham et al. 2011) to select a GAMA group to test our PSF models and make a preliminary IHL estimation. This catalogue overlaps with HSC-SSP PDR3 in the GAMA-fields G09, G12 & G15, and partially overlaps in G02. For the purpose of this work, we only use the HSC data that overlaps with GAMA. The HSC star images from the overlapped regions are deemed sufficient for reconstructing the PSFs (see Section 4.2 for further details).

2.1 The Hyper Suprime-Cam SSP Survey

The Hyper Suprime-Cam is an optical-infrared imaging camera mounted on the prime focus of the 8.2-meter Subaru Telescope. It is operated by the National Astronomical Observatory of Japan (NAOJ) and is located at the Mauna Kea Observatory in Hawaii. The large focal plane is paved with a mosaic of 116 charge-couple devices (CCDs) detector formatting $2\text{k} \times 4\text{k}$, covering a field of view of $\sim 1.7 \text{ deg}^2$ with a pixel scale of $\sim 0.168 \text{ arcseconds}$.

HSC-SSP consists of three layers (Wide, Deep & UltraDeep) and uses five broad-band (*griZY*) and four narrow-band filters. Each of the layers has a different sky coverage and depth: 1400 deg^2 ($r \sim 26 \text{ mag}$), 27 deg^2 ($r \sim 27 \text{ mag}$), and 3.5 deg^2 ($r \sim 28 \text{ mag}$) for the Wide, Deep, and UltraDeep layers respectively. The Wide layer consists of three fields covering 916 pointings in total: HECTOMAP, Spring, and Autumn, which were selected to overlap other multi-wavelength surveys to maximise the scientific synergy with HSC. In addition, AEGIS (Davis et al. 2007) is a single pointing to Wide layer depth used for calibrating photometric redshifts. The Deep layer consists of four fields: XMM-LSS (XMM Large Scale Structure survey, Pierre et al. 2004), Extended-COSMOS (E-COSMOS, Aihara et al. 2018), ELAIS-N1 (European Large Area ISO Survey, Oliver et al. 2000) and DEEP2-F3 (Newman et al. 2013). E-COSMOS, DEEP2-3 and ELAIS-N1 each have four pointings, while XMM-LSS has three. HSC-SSP also covers two UltraDeep fields: COSMOS (Cosmic Evolution Survey, Scoville 2007), which consists of one single pointing centred and partially overlapped with the E-COSMOS Deep field, and SXDS (Subaru/XMM-Newton Deep Survey, Furusawa et al. 2008), one pointing located in the western extreme of XMM-LSS and partially overlapped with this field.

2.1.1 PDR3

To date, the HSC-SSP has three public releases: PDR1 (Aihara et al. 2018), PDR2 (Aihara et al. 2019) and PDR3 (Aihara et al. 2022). Every new PDR is a major update in terms of depth and area in comparison to their predecessors. In addition, a significant number of improvements in the data processing HSC pipeline have taken place since HSC-SSP PDR1 data was released, with careful consideration of the sky estimation capabilities (Kelvin et al. 2023). The sky background estimation remains one of the challenges in low surface brightness imaging and is one of the major sources of systematics (Fliri & Trujillo 2016; Mihos et al. 2017; Liu et al. 2023).

PDR1 over-subtracted the sky around the extended wings of stars and bright galaxies, and this issue was mitigated by a global sky subtraction introduced in PDR2 (see Figure 5 of Aihara et al. 2019). The improved pipeline subtracted the background using superpixels of $1\text{k} \times 1\text{k}$ pixels ($\sim 168''$ on a side). Among the biggest changes

between PDR2 and PDR3, the newest pipeline also performs a global sky subtraction for extended object science, but this time the sky subtraction consists of gridding a visit image into superpixels of $8\text{k} \times 8\text{k}$ ($\sim 23''$ on a side). However, false detections and measurement failures around the extended wings of bright stars and galaxies were still present in PDR3 and made the authors add a second local sky subtraction using 256×256 superpixels ($\sim 43''$ on a side). Following this idea, there are two types of coadd images in PDR3: the first with both sky subtractions applied, and the second with only the global sky subtraction. As we are interested in studying the intra-halo light surrounding extended objects, we need the well-preserved wings of the HSC bright star images to reconstruct extended PSFs. For this reason, we decide to work with the latter type of coadded image. This intermediate-stage data is not publicly available on the HSC-SSP website via the Data Archive System (DAS) search tool and we contacted the HSC software team to download it. For the reconstruction of the HSC-SSP PDR3 PSFs we only use the HSC-SSP PDR3 data that is overlapped with GAMA, which amounts to $\sim 8 \text{ TB}$ of data.

2.2 The GAMA galaxy group catalogue G³Cv10

GAMA is a spectroscopic and photometric survey of $\sim 330,000$ galaxies down to a depth magnitude limit of $r < 19.8 \text{ mag}$ over $\sim 250 \text{ deg}^2$ (Driver et al. 2011; Liske et al. 2015; Driver et al. 2022). The survey was carried out over seven years using the optical AAOmega multi-object spectrograph on the 3.9-meter Anglo-Australian Telescope (AAT) at the Siding Spring Observatory. The area coverage is split into five regions: three equatorial fields (G09, G12, and G15) and two southern fields (G02 and G23).

One of the key benefits of this survey is its high spectral completeness of $\sim 98\%$ (Robotham et al. 2010; Baldry et al. 2010; Driver et al. 2022). This enables us to make a statistically significant analysis of galaxy environments, including low mass groups ($M < 10^{13} \text{ h}^{-1} \text{ M}_\odot$). Along with this increased redshift density, GAMA also provides multiple bands of imaging data covering the ultraviolet to far infrared.

The quality of this data, allowed Robotham et al. 2011 to create the GAMA galaxy group catalogue G³Cv10. This catalogue is built on a friend-of-friends (FOF) linking algorithm, which determines whether galaxies are associated with one another based on both their projected and comoving separations. The parameters of this algorithm were determined by comparing to a set of mock GAMA galaxy catalogues obtained from populating the Millennium dark-matter simulations (Springel et al. 2005) with galaxies using the GALFORM (Bower et al. 2006) semi-analytic model.

G³Cv10 contains 26194 galaxy groups (with 2 or more members) located at the GAMA II equatorial (Liske et al. 2015) and G02 survey regions. Some of the listed properties for each group in G³Cv10 are the halo mass, multiplicity, redshift, total *r*-band luminosity, size, position, velocity dispersion, and identification of its Brightest Group Galaxy (BGG) originally defined in the *r*-band.

The regions where HSC-SSP PDR3 and GAMA overlap are shown in Fig. 1, where the total overlapping area consists of $\approx 200 \text{ deg}^2$. The HSC Wide layer is indicated in pale blue, the Deep layer is indicated by blue-filled circles, and the UltraDeep layer is represented by dark blue single pointings. GAMA regions are shown in pale red.

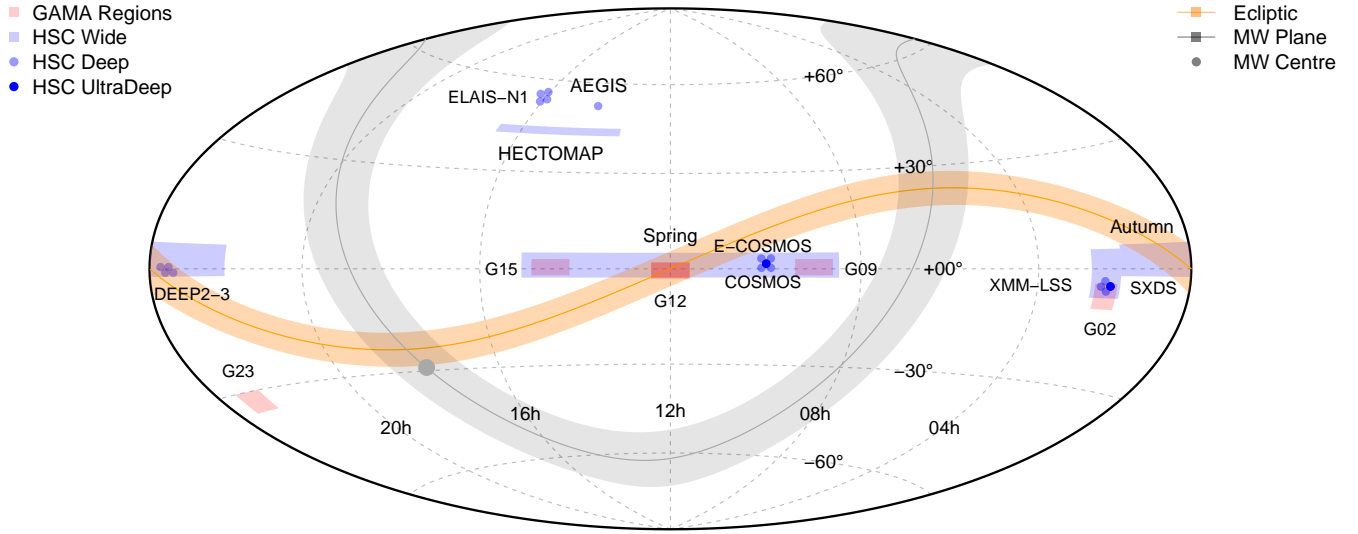


Figure 1. Location of the HSC-Wide (pale blue), Deep (blue), and UltraDeep fields (dark blue) and the GAMA fields (pale red) on the sky in equatorial coordinates. The grey shadow represents the Milky Way (MW) plane and the centre of the MW is indicated by the grey-filled circle. The orange shadow indicates the ecliptic plane.

3 HSC-SSP PDR3 PSF DERIVATION

We apply an empirical method to construct the PSF for the HSC-SSP PDR3 in each of the five g,r,i,Z and Y bands. For each HSC band, we create a PSF in each of the four G02, G09, G12, and G15 GAMA regions (we do not have HSC observations in G23). We construct different PSFs in different regions to assess their stability across space and time. Once we have the PSFs per region and filter, we combine them across different regions and same filter in order to obtain the final PSFs for each HSC band. This is appropriate as, shown later, there is little variation in each PSF across the GAMA regions.

3.1 Star selection

We follow a similar approach to Infante-Sainz et al. 2020, where the authors originally constructed a PSF for the SDSS. This method consists of reconstructing different parts of the PSF by the median-clipping stacking of stars within a wide brightness range. In particular, the authors divide the PSF construction into three parts. Bright and saturated stars are used to characterise the outer part (or wings) of the PSF, stars of intermediate brightness are used for the middle part and the core is characterised by non-saturated faint stars. As the central pixels of bright stars are highly affected by the saturation of the CCD dynamical range, the authors only use the outer pixels of these images to create the faint PSF wings. However, the central pixels of fainter stars are unaffected by saturation and can be used to reconstruct the PSF core.

Based on our own experimentation, in this work we divide the PSF into four radial regions: outer, middle, inner, and core, where each part has a different brightness level. These four selected magnitude ranges are:

- Outer: $\text{mag}_{\star,g} < 8$
- Middle: $11 < \text{mag}_{\star,g} < 11.5$
- Inner: $14 < \text{mag}_{\star,g} < 14.1$
- Core: $18 < \text{mag}_{\star,g} < 18.02$

GAMA region	Outer	Middle	Inner	Core
G02	28	240	259	225
G09	98	753	1064	1034
G12	68	347	478	518
G15	69	447	515	762

Table 1. Quantity of stars per GAMA region in the HSC g -band that was selected to reconstruct the different parts of the PSF. A similar amount of stars were used for the construction of the PSFs in the rest of the HSC filters.

As previously mentioned, we use the Gaia Data Release 3 catalogue (Gaia Collaboration et al. 2022) to identify stars that satisfy these magnitude requirements in each of the HSC-SSP PDR3 and GAMA overlap regions (using the g -band data of the catalogue). The images of the stars are from the overlapping regions between HSC-SSP PDR3 and GAMA. We verify that this selection contains enough stars to accurately reconstruct the PSF by including extra HSC data and showing that it does not improve our results (this idea is discussed in detail in Sec. 4.2).

We then also apply an additional constraint that rejects the stars that are not within one degree of radial distance from the centre of any HSC image. By doing this, we avoid distortion problems around the borders of the images. The resulting number of stars per region is similar from band to band, where slight changes in the quantity are due to small coverage differences between the five HSC filters. Table 1 shows the number of stars that were used to reconstruct each part of the PSF in the g -band per GAMA field.

The size of each HSC cutout used to reconstruct the outer PSF is $4k \times 4k \text{ pix}^2$, meaning that after applying the stacking and combination process (see below for full details), the resulting PSFs extend to a radius of $R = 2000$ pixels (5.6 arcmin) in all the five bands. As the rest of the selected stars are used to reconstruct the inner parts of the PSF, the cutout sizes are smaller: $R = 1000$ pixels for the middle

stack, $R = 500$ pixels for the inner stack, and $R = 200$ pixels for the core one.

We have made available the PSF reconstruction scripts written in the open-source R language at https://github.com/luciagarate/HSC_PSFs. This consists of three scripts: the first describes the selection of the star images for each PSF region and subsequently stacking (Section 3.2), the second describes the combination of the 4 regions to reconstruct a PSF per GAMA region and HSC filter (Section 3.3), and the third describes the process to reconstruct the final PSFs (Section 3.4). The HSC-SSP PDR3 PSFs in all five bands are also available publicly as FITS files.

3.2 Stacking

After selecting stars and generating cutout HSC images per GAMA region and filter, we proceed to reconstruct the different parts of the HSC PSF. Section 3.2.1 explains how we build the outer part of the PSF. Section 3.2.2 describes the steps we followed to build the middle and inner parts of the PSF, and Section 3.2.3 contains the details about the construction of the core.

3.2.1 Outer part of the PSF

We use stars with a magnitude brighter than $m_g = 8$ for the PSF wings. The second column in Table 1 shows the number of stars used to reconstruct the outer PSF region in the g -band, where G02 has the lowest number because we only use the HSC (Wide) data that overlaps with GAMA.

To reconstruct the outer part of the PSF we apply a median stacking process to all the selected stars images. This is done with the warping and stacking package PROPANE¹, written in the open-source R language. As we use a median stacking technique that naturally ignores the bright pixels from the background sources, a masking process is not necessary in the stacking step. However, we take the additional precaution of masking the bright background sources to calculate the normalisation value in each image. Before stacking, we normalise each image by the value of the median flux contained in an annulus situated between 400 and 410 pixels from the centre of the bright star. The position of the annulus was chosen to be as close to the centre as possible but avoiding the central saturated region of each image. The width of the annulus was selected in order to get a good signal-to-noise ratio (S/N).

To mask the star images in the normalisation step we use the PROFOUND² (Robotham et al. 2018) source finding and photometry analysis package. PROFOUND detects sources using dilated segments (isophotal outlines) of arbitrary shape (rather than elliptical apertures) and measures statistics like flux, size, and ellipticity. In particular, we run the `profoundImDiff` function on the star image, which creates another image that is the result of the original minus a smoothed version (in this version the borders of the segmentation maps have no abrupt changes). The parameter that establishes the standard deviation of the blur is `sigma`. We then apply the `profoundDilate` function to the resulting image, which dilates the segmentation maps by typically 30%. During the dilation process, a watershed de-blending approach is taken, where the segments are not allowed to overlap. The dilation is important to make sure that the background sources are completely masked. The `size` parameter controls the width/diameter

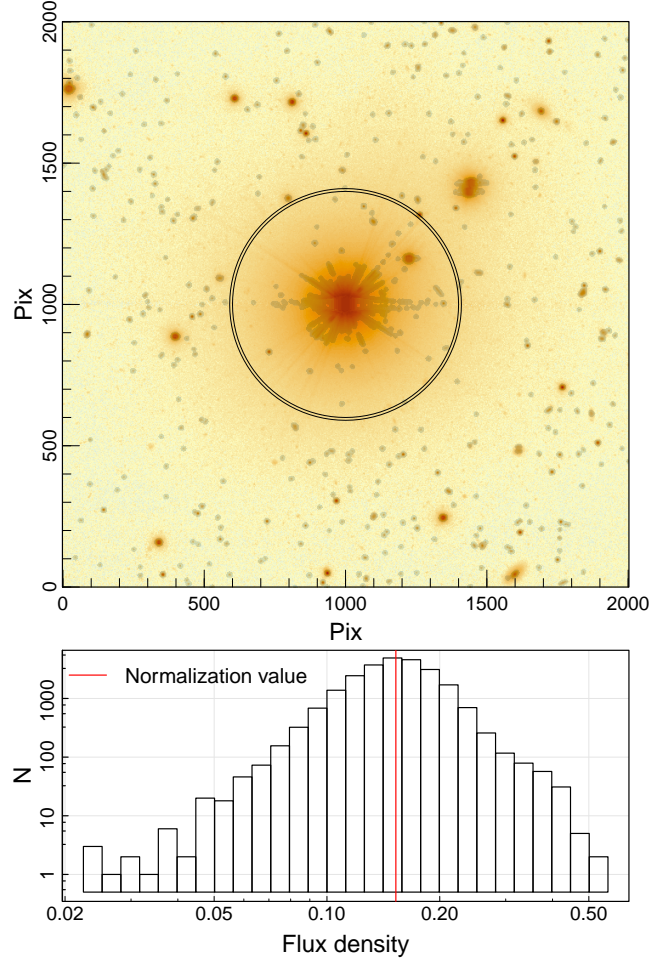


Figure 2. Upper: image of a star used to reconstruct the PSF outer part where the PROFOUND masks are indicated by the semi-transparent gray spots. The normalisation annulus used to stack all the images is delimited by the two black thin circles. Lower: histogram of the flux values of all the pixels within the annulus from the upper image, where the red vertical line indicates the median value of this distribution.

of the dilation kernel in pixels. For the outer stack, we create the dilated segmentation maps with `sigma = 2` and `size = 21` and we then mask all of the pixels inside each segment. The upper Fig. 2 shows an image of a star used to reconstruct the outer part of the PSF with the corresponding masks. The black circles show the normalisation annulus. As we are calculating the median flux inside the annulus, our masking approach is not very aggressive. The lower plot shows a histogram of the pixel flux values within the annulus of the upper image, where the vertical red line indicates the median value used to normalise the flux. Images -where the total masked area is more than 80%- are discarded for the stacking process. Finally, we proceed to make a median stack of the unmasked normalised images with the `propaneStackFlatFunc` function, which stacks already aligned (flat) images. The same normalisation process is applied in all the HSC filters.

In order to be cautious, we also calculate the median stacks with the masked star images and conclude that the PSF reconstructed with the median unmasked stacking technique achieves a higher signal-to-noise ratio without biasing the result. This comparison is discussed in more detail in Section 4.3.

¹ <https://github.com/asgr/ProPanE>

² <https://github.com/asgr/ProFound>

The leftmost panel of Fig. 3 shows the stack of the stars used to reconstruct the PSF outer part with the selected annulus for the normalisation.

3.2.2 Middle and Inner parts of the PSF

The methodology to construct the middle part of the PSF is similar to that in Sec. 3.2.1. The main difference is in the normalisation step, where we select the annulus of inner radial distance 200 pixels from the centre and width 20 pixels. In addition, the size of each image used is $1\text{k} \times 1\text{k}$ pix 2 , and images, where the masked area is more than 50%, are not considered for the stacking process.

In the case of the inner PSF reconstruction step, the size of each image is 500×500 pix 2 , and the normalisation annulus has an inner radius of 100 pixels and an outer radius of 140 pixels. To stack, we only select the images of stars that have less than 2% of pixels masked. We then proceed to apply the median stack with the unmasked images.

The selected `sigma` and `size` values for each filter and region are indicated in the script "1_Stacking.R" at https://github.com/luciagarate/HSC_PSFs. The middle and inner stacks with their respective selected annuli are shown on the second and third panels of Fig. 3.

3.2.3 Core of the PSF

The inner radius of the annulus for the normalisation step in the core stack is 50 pixels and the outer is 100 pixels, where the size of each image is 200×200 pix 2 . In this case, the masks for the normalisation step are calculated using the main function of PROFOUND, `profoundProFound`. This function offers great flexibility to create large segments around background sources, which is important for this step due to the faintness of the central star. Images that were selected for the stacking process have less than 20% of pixels masked. We also discard the stars that do not have the brightest pixel in the centre of the image. Due to GAIA coordinate errors, it is possible for the brightest pixel of the HSC image to be uncentred. Such cases are removed (we only want stars with low proper motion). As in the other three cases, we calculate the median stack with the selected unmasked images of the stars.

The rightmost panel of Fig. 3 shows the core stack with the selected annulus to normalise the images.

3.3 Combination

The four separate median stacks are combined in order to obtain the final HSC PSF per band and GAMA region.

We begin by combining the outer and middle stacks. To combine both parts, we first normalise them separately by calculating the median flux within an annulus of an inner radius of 150 pixels and an outer radius of 160 pixels in each stack. We then replace inside a circle of radius 150 pix in the outer stack pixels from the middle stack, henceforth outer + middle. Similarly, we combine the outer + middle with the inner stack, and finally the outer + middle + inner with the core stack. The selected annuli to normalise the different parts are indicated in Table 2, as well as the chosen radii to combine them.

The values of the annuli to normalise each image and radii to combine the regions were chosen by analysing the 1-D radial profile of each stack, where we look for the brightest inner radius that has a good S/N in both parts and where the merging profiles agree well. We show the step-by-step 1-D radial profiles of the combined stacks

in the left panel of Fig. 4, and the 1-D radial profiles of the single PSF stacks in the right panel³. The salmon line in the first panel is the 1-D radial profile of the outer stack, whereas the blue line represents the 1-D profile of the outer and middle stack combination. The radius of this junction (150 pixels) is indicated with the right dashed grey line. Following this idea, the green line represents the combination of the three outer parts, and the purple one is the final combination. The 60 and 20-pixel junction radii are indicated by the middle and left dashed grey lines respectively. All the selected annuli to normalise and radii to replace are the same across the five HSC filters. In the second panel of Fig. 4, we show the 1-D radial profiles of the median single PSF stacks, where each point represents each pixel of the selected PSF region. The salmon points represent the outer region of the PSF, the blue and green points are the pixels from the middle and inner PSF regions parts respectively, whereas the purple points represent the core of the PSF. We also show the flux error associated with each of the four median stacks in pale blue. The errors are estimated by calculating the 1σ -quantile (half of the range containing the central 68% of data) of each stacked pixel divided by the square root of the number of images within each stack (see Table 1 for reference).

The spread in the flux pixels values of the 1-D radial profiles at $R > 1000$ pix is a factor or ~ 4.85 larger than the median of the stacking error associated with each individual pixel. In principle, the large scatter could be related to two different error sources: low signal-to-noise ratio and systematic uncertainties. In Sec. 4, we verify that adding more data does not improve the S/N at large radii in the resulting PSFs (i.e. the value of the quantitative scatter does not vary), suggesting systematic uncertainties in the background subtraction process are the only cause of the spreads in the PSF 1-D radial profiles at $R > 1000$ pix.

Fig. 5 shows the images of the above-mentioned combinations for the different parts: the first panel is the outer stack, the combination of the outer and middle parts is shown in the second panel, the third panel shows the combination of the two outer parts with the inner one and the final combination is shown in the fourth panel.

After combining the four median stacks, we obtain the HSC PSFs with a radial extension of ~ 5.6 arcmin. We then proceed to apply the next two final details to each of the PSFs in order to obtain the final HSC PSFs per band and GAMA region:

- We apply a symmetric process by making horizontal, vertical and diagonal reflections to obtain a symmetric 2-D PSF. To do this, we create a new image with the same dimension as the original PSF. For each pixel in the new image, we sum its original value with the values of the three reflected pixels values: the horizontally reflected pixel, the vertically reflected, and the diagonally reflected one.
- We then normalise the flux of each PSF image by making the sum of all the pixel values equal to one.

The script of the PSF combination process is available as "2_Combining.R" at https://github.com/luciagarate/HSC_PSFs. The rightmost panel of Fig. 5 shows the extended *g*-band HSC PSF in the GAMA region G15 after applying the final details.

3.4 Final stack

We reconstruct the HSC-SSP PDR3 PSFs per band and GAMA region, resulting in four PSFs for each of the five filters. We proceed

³ The 1-D radial profiles are made with the flux and radius values of all the pixels of the respective PSF stack, therefore they are not radially-averaged profiles.

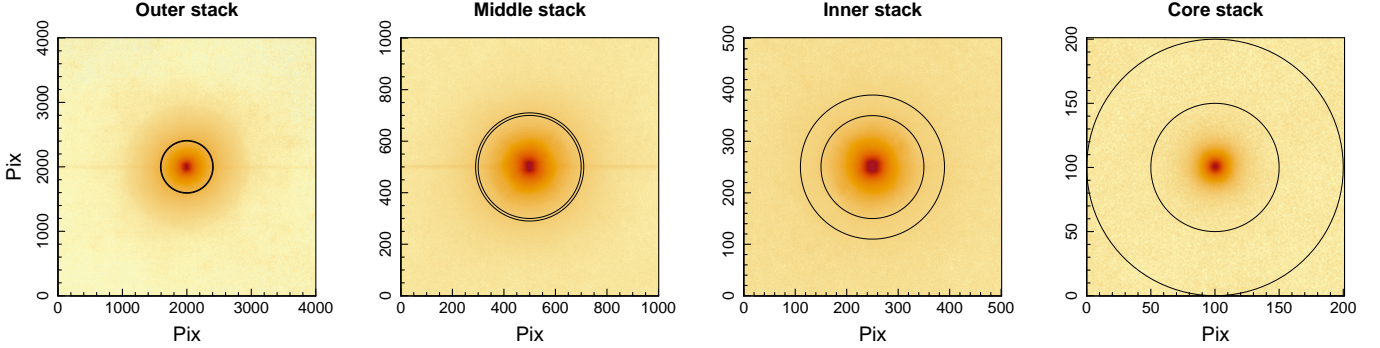


Figure 3. First panel shows the outer stack, the second panel shows the middle stack, and the third and fourth panels are the inner and core stacks, all with their respective chosen annuli to normalise each star image indicated by thin black circles. The sizes of the respective stacks are: $4k \times 4k \text{ pix}^2$, $1k \times 1k \text{ pix}^2$, $500 \times 500 \text{ pix}^2$ and $200 \times 200 \text{ pix}^2$. All the images are from the G15 region in the g -band.

	Normalisation annulus	Combination radius
Outer	160-150	150
Middle	160-150	
Outer + Middle	70-60	60
Inner	70-60	
Outer + Middle + Inner	30-20	20
Core	30-20	

Table 2. Quantity of stars per GAMA region in the HSC g -band that was selected to reconstruct the different parts of the PSF. A similar amount of stars were used for the construction of the PSFs in the rest of the HSC bands.

to reconstruct the final extended HSC-SSP PDR3 PSFs by median stacking the PSFs within the same band. In the left panel of Fig. 6 we show the final g -band HSC PSF image up to $R \sim 5.6$ arcmin (2000 pixels). In the right panel, we show its 1-D flux radial profile, where the horizontal dashed line indicates the maximum flux value of the PSF divided by two ($f_{\max}/2$), and the vertical one is indicating the full width at half maximum (FWHM) of the PSF also divided by two. In the g -band, the FWHM is 0.772 arcsec (~ 4 pixels). The difference in flux between the peak and the minimum value is $\Delta\text{flux} \sim 10^8$, which is equivalent to $\Delta\text{mag} \sim 20$.

In the left panel of Fig. 6 we can easily identify some of the CCD artefacts (mainly more remarkable around bright stars) described in Aihara et al. 2022. These artefacts are unwanted or unintended effects that occur in CCD images (noise, blooming, hot pixels, dead pixels, etc) where some of them are identified and interpolated over in the CCD processing, but some artefacts may still be present in the processed images.

The bleeding (or blooming) due to CCD saturation is the horizontal feature that is present in all five bands (see Appendix A). We see this feature not only in the outer stack but also when stacking the stars from the middle region and even when stacking the inner region in some of the bands. Another observable artefact in Fig. 6 is the smooth halo component around the centre of the PSF, which is also present in all the stacks. The HSC-SSP PDR3 PSFs in the other four bands are shown in Appendix A.

In Fig. 7 we compare our r -band HSC-SSP PDR3 PSF flux profile (dark blue) + extrapolated dashed red line up to 50 arcmin versus the r -band PSF flux profiles of the 0.9 m Burrell Schmidt telescope (pink, Slater et al. 2009) and the Dragonfly Telephoto Array (green, Abraham & van Dokkum 2014). The three profiles were normalised

to have a flux equal to one within the range of 0.1 and 5 arcmin and the minimum radius plotted is 0.1 arcmin. In all three PSFs, more than 90% of the total flux is contained at $R < 0.1$ arcmin (Abraham & van Dokkum 2014), with our PSF accounting for 97.2% of the total light within $R < 0.1'$. This means that less than $\sim 3\%$ of the total flux is contained in the extended wings of the HSC-SSP PDR3 PSF. Both the Burrell Schmidt telescope and Dragonfly Telephoto Array are highly optimized for low surface brightness imaging and have well-behaved PSFs out to large radii. In comparison to them, we find the performance of our HSC-PDR3 PSF to be remarkably good.

4 TESTS

We run a number of tests to demonstrate the validity of the choices made during the PSF reconstruction process. We first test the stability across time and space of our PSFs by comparing the reconstructed PSFs per GAMA field with the final PSF in each band. We then check that the number of stars with $\text{mag}_{\star,g} < 8$ per filter and GAMA region is optimal to reconstruct the outer part of the PSF. Finally, we verify that the resulting PSFs when using unmasked images achieve a higher signal-to-noise ratio at large radii than the PSFs made with masked images.

4.1 PSF temporal and spatial stability

As mentioned before in Sec. 3.3, the PSF reconstruction process begins with creating a PSF per GAMA field and then stacking the four PSFs per band to create the final one. In order to test the PSF

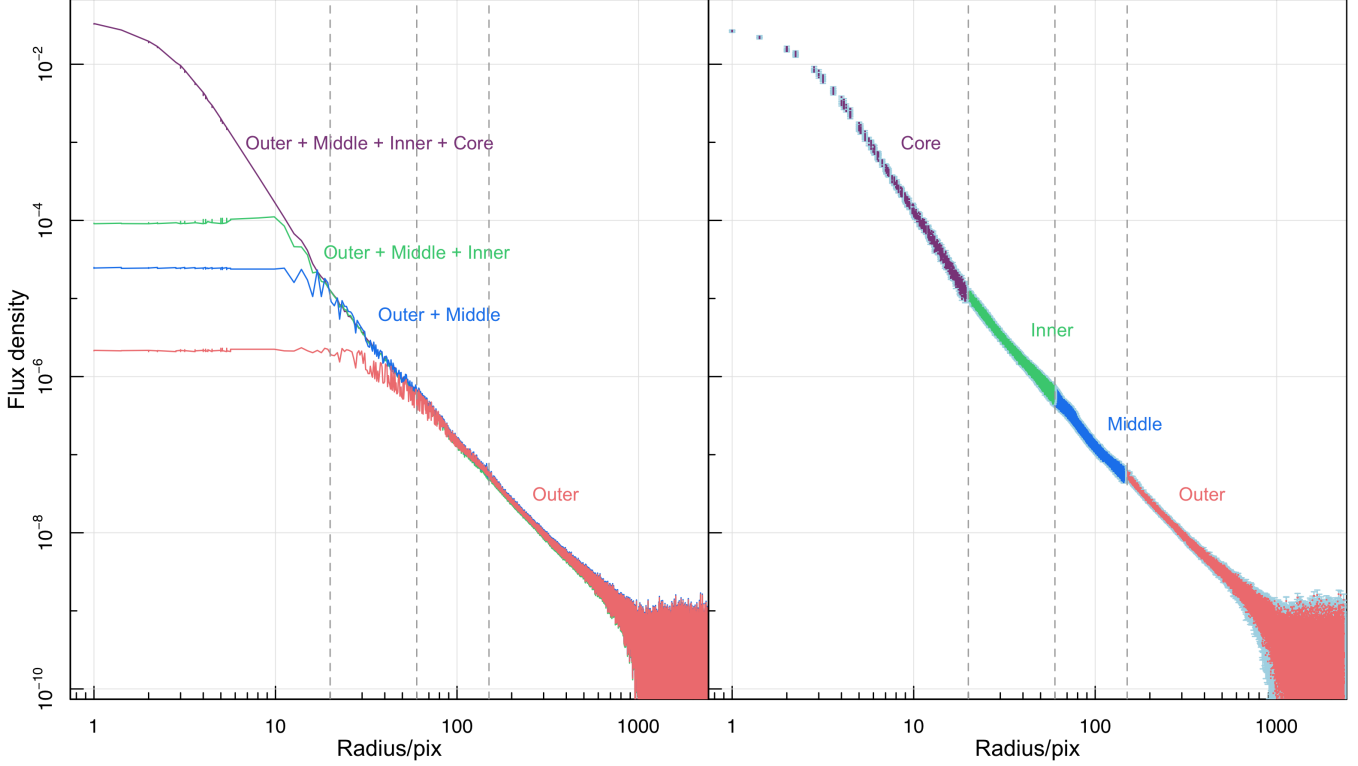


Figure 4. First panel: 1-D radial profiles of the outer stack (salmon), the combination of the outer and middle stacks (blue), the combination of the outer, middle, and inner stacks (green), and the combination of the outer, middle, inner and core stacks (purple), which is the final HSC *g*-band PSF. Second panel: 1-D radial profiles of the individual stacks, where the outer stack is represented by the purple points, the middle stack by the blue points, the inner stack is indicated by the green points, and the core stack by the orange points. We also show the flux stack error per pixel associated with each of the four median stacks, where the error is calculated as the 1σ -quantile divided by the square-root of the number of images within each stack. In both panels, the right dashed grey line indicates the radius where we make the first combination (150 pix), the middle one indicates the radius where we join together the outer + middle with the inner stack (60 pix) and the left one indicates the radius where this combination and the core stack are combined (20 pix). The profiles are made with observations from the G15 GAMA region in the *g*-band.

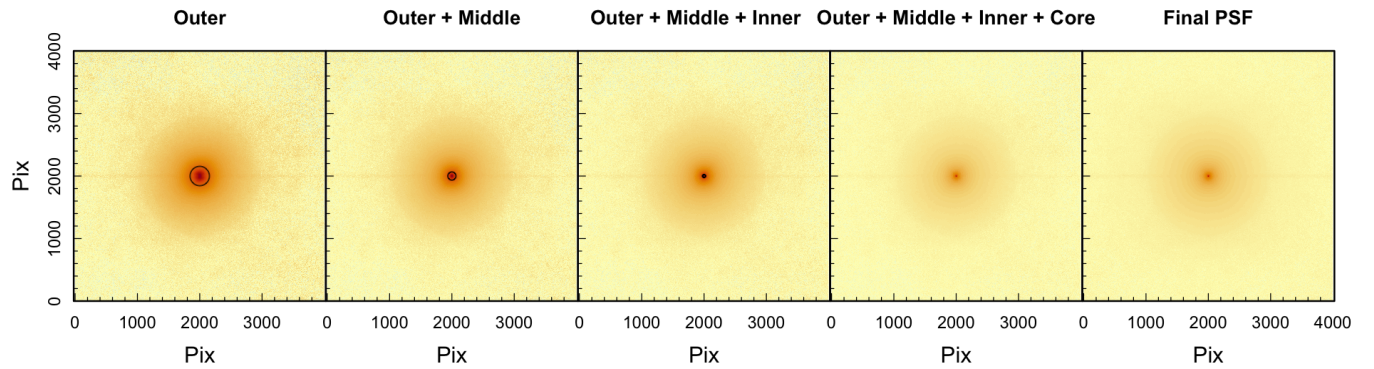


Figure 5. Left panel: outer PSF stack, where the annulus that was selected to normalise both outer and middle stacks is represented by the two thin black circles. The inner radius (150 pix) delimits the pixels that we replace with the middle stack. Second panel: outer + middle combination with the annulus of outer radius 70 pix and inner one 60 pix, where we replace the inner stack. Middle panel: outer + middle + inner combination with the annulus situated between 30 and 20 pixels from the centre of the image, where we replace with the core stack inside the black circle delimited by the inner radius. Fourth panel: HSC *g*-band PSF before applying the final details (normalisation + symmetrisation). Right panel: HSC *g*-band PSF after applying the final details. All the observations are from the G15 GAMA region.

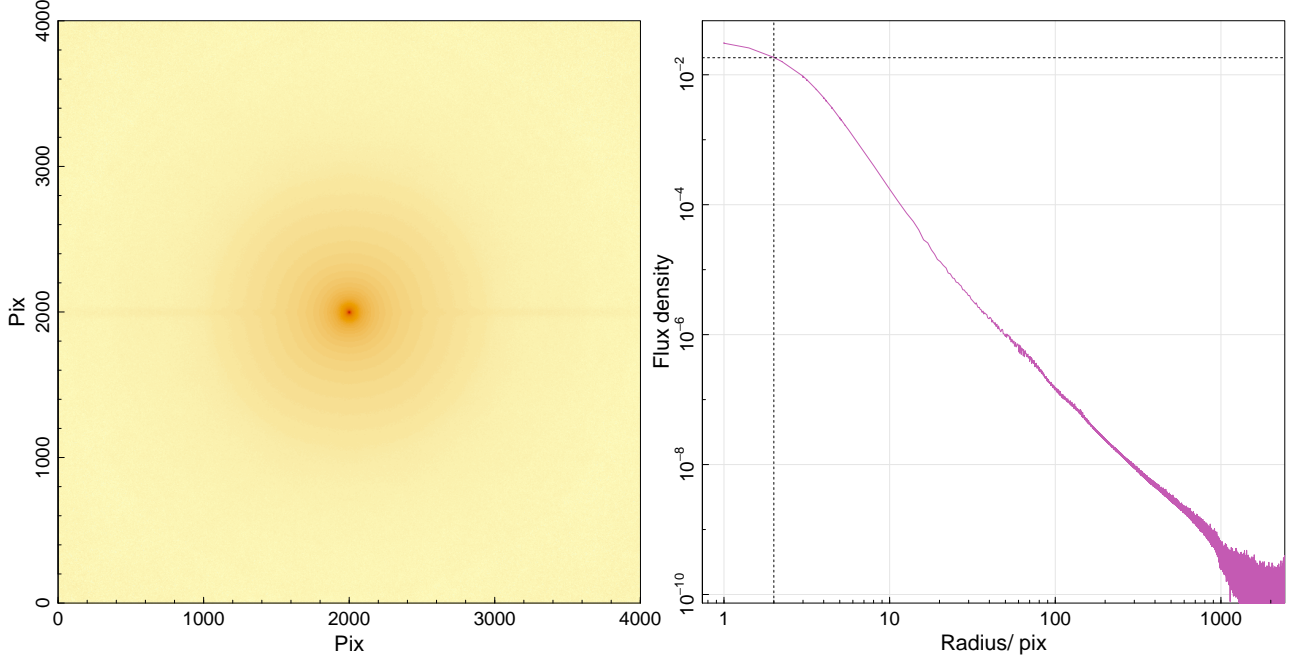


Figure 6. HSC-SSP PDR3 PSF in the *g*-band. The left panel is the image of the PSF and the right panel is the 1-D radial profile. The PSF is normalised to have a total flux equal to one. The horizontal dashed line indicates the $f_{\max}/2$ of the profile, where f_{\max} is the maximum flux value, and the FWHM/2 (~ 0.772 arcsec) is specified by the vertical dashed line.

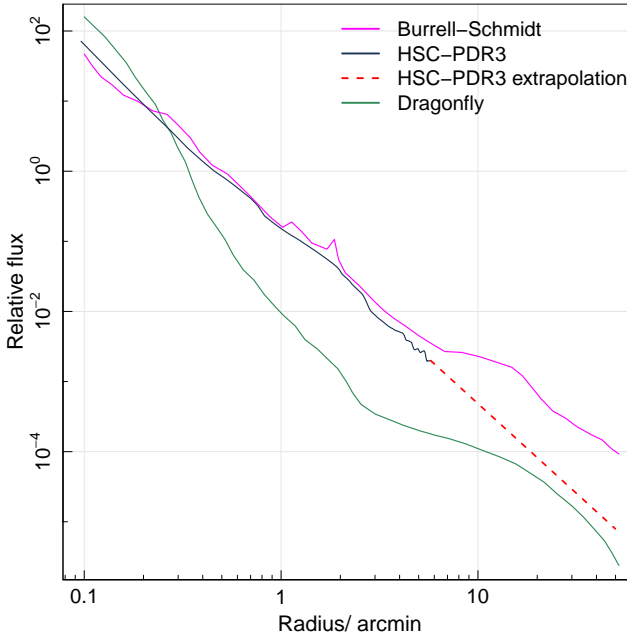


Figure 7. Comparison of the *r*-band PSF radial profiles of Burrell Schmidt telescope (pink), Dragonfly Telephoto Array (green), and our HSC-PDR3 model (dark blue) with an extrapolation up to 50 arcmin shown as the red dashed line. Each of the profiles is normalised so that the flux between 0.1 arcmin and 5 arcmin is one.

performance, we analyse the differences of each reconstructed PSF per GAMA region relative to the final PSF. To quantify this difference we use the percentage error:

$$\frac{GXX_{\text{data}} - \text{Final}_{\text{model}}}{\text{Final}_{\text{model}}}, \quad (1)$$

where GXX_{data} represents the PSF from each GAMA field GXX and $\text{Final}_{\text{model}}$ is a model of the final PSF. In Fig. 8 we show the percentage difference between the *g*-band PSFs of each GAMA field and the *g*-band final HSC PSF model. The pink inset enlarges the profiles at the sub-1% level, to show the tiny differences. Only slight PSF variations over the GAMA regions are present in the *g*-band and also in the rest of the filters, indicating temporal and spatial stability. Note that G02 has more scatter at large radii due to the lower quantity of stars that contribute to the outer stack (we only use data where GAMA and HSC overlap, and in the case of G02 they only partially overlap).

4.2 Outer stack

Compared to the stars of the middle, inner, and core regions, the quantity of bright stars ($\text{mag}_{\star,g} < 8$) across all five filters is considerably lower (see Table 1). To check whether more bright stars will improve the PSF S/N at large radii, we reconstruct the outer PSF with all the stars in HSC Wide that satisfy the condition $\text{mag}_{\star} < 8$, comparing it to the outer PSF created with only the $\text{mag}_{\star} < 8$ stars from the overlapped regions between HSC Wide and GAMA. To find all the bright stars in the Spring, Autumn, and HECTOMAP fields (i.e. HSC Wide), we also make use of the Gaia Data Release 3 catalogue. The resulting number of bright stars in HSC Wide per filter is ~ 1740 . This analysis is only done in the *g*-band.

We verify that increasing the number of bright stars makes no significant improvement in the signal-to-noise ratio of the PSF. In Fig. 9 we express the differences between both *g*-band outer stacks by showing the percentage error of each outer stack and the final

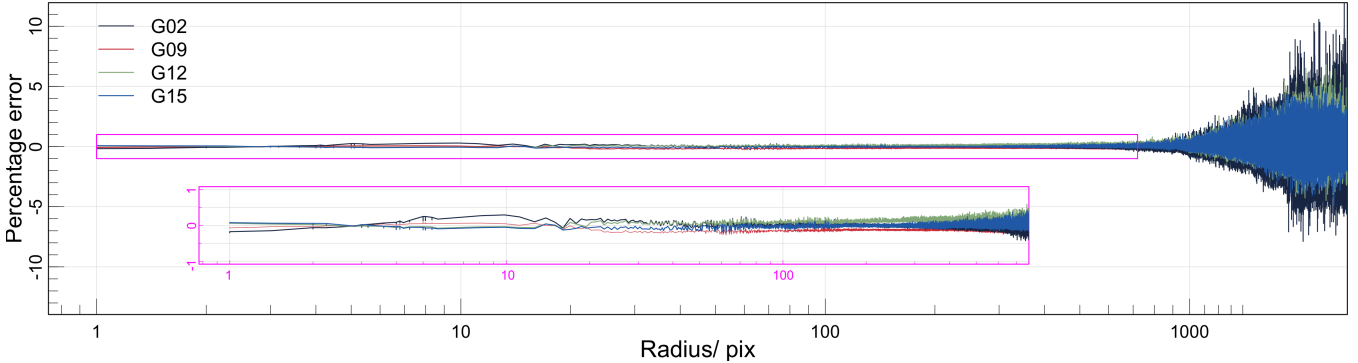


Figure 8. Percentage error between each GAMA-field PSF and a model for the final PSF in the g -band, where different line colours correspond to the different GAMA regions. The rectangular pink box presents a zoomed-in view between 1 and 1000 pix on the x-axis and between -1 and 1 on the y-axis. The G02 PSF has more scatter because the number of stars in the overlapped region between G02 and HSC-Wide is smaller.

HSC PSF model $\text{Final}_{\text{model}}$ mentioned in Sec. 4.1 (in this model the outer stack is created with $m_g < 8$ stars from HSC Wide \cap GAMA). The blue curve shows the percentage error that compares the outer stack created with ~ 1740 stars (all $m_g < 8$ stars from HSC Wide) and the model. The pink curve shows the percentage error between the outer stack created with the ~ 270 $m_g < 8$ HSC Wide \cap GAMA stars and the model itself. The big spread in both curves at large radii is probably caused by background subtraction systematics. Since there are no clear improvements observed by stacking a higher quantity of stars, we decide to continue working with the simplest case: the outer region made of only the stars from the overlapping areas between HSC and GAMA.

4.3 Stacking technique

We use the median statistic estimator to stack the unmasked images, as this is not heavily biased by the higher flux value pixels of the background objects. Additionally, the process of robustly masking sources may be problematic and induce errors. When applying aggressive object masks in order to be robust against biases, surrounding halo pixels from the central stars could also be masked (reducing the S/N).

To demonstrate the robustness of our approach, we reconstruct an HSC PSF where all the median stacks were made with the background-masked star images. The masks are created in exactly the same way as in the normalisation step: by making use of the `profoundImDiff` and `profoundDilate` functions from the PROFOUND package. We then compare the PSF made with the masked images and the PSF made with the unmasked images per GAMA field. Fig. 10 shows the relative difference between both PSFs and the model of the final PSF $\text{Final}_{\text{model}}$ (created by stacking the PSFs from each GAMA field and using the unmasking technique) in the g -band. Each panel indicates one GAMA region, with the blue percentage error curve coming from the PSF made with the masked images and the salmon curve coming from the PSF where the star images were unmasked. In all four panels, the salmon curves are less noisy across the different stacks (the junction radii of the four stacks are delimited by the dashed black lines) and appear to be smoother. The maximum relative difference in the g -band is 1%, which represents the best-case scenario compared with the other bands, as in the r -band this percentage goes up to 3% and up to 4% in the rest of the filters. This comparison confirms that stacking the unmasked star images with a median technique leads to PSFs with a better signal-to-noise ratio than the PSFs generated when we apply a median stack

to the background-masked images. Improving the S/N via masking would require additional effort and time for probably little gain.

5 PSF APPLICATIONS

In this section, we show two examples of our new HSC-SSP PDR3 PSFs performance when used in scientific applications. The first example consists of using our empirical PSFs to generate a two-dimensional model of an HSC-PDR3 star image. Additionally, we use the PSFs to model and remove the scattered light in an image of a GAMA group of 14 galaxies situated in the HSC UD SXDS field.

5.1 Star application

In the first application, we use the HSC-SSP PDR3 PSFs to fit a two-dimensional model per band to HSC-PDR3 observations of a bright star located in G09. The images of this star in the five different HSC filters are shown in the first row of Fig. 11. The next row shows the masked version of these images, where we use the PROFOUND package to mask the background sources and the cores of the stars. The central part of each image is masked up to a radius where the pixels are no longer saturated. This masking limit can easily be determined by plotting the star profiles. The reason behind avoiding the saturated pixel values is that they introduce fake flux measurements and could have a dramatic effect on the subsequent star profiling. Once we have correctly masked the images, we proceed to make the 2-D photometric star profile modelings with ProFit⁴ (Robotham et al. 2017). We use this Bayesian 2-D galaxy profiling tool to generate a star model per band, where we make use of the already parameterized point-source profile function from the libProFit library. In this case, the only free parameter in the model that we fit is the star magnitude. We then use the `profiltMakeModel` function, which gives us the option to specify the PSF model (our empirical HSC-SSP PDR3 PSFs images) that gives the shape to the star profiles. In this step, the PSF images are renormalized to ensure the flux contained per band is correct given the magnitude zero-point of HSC ($m_{\text{zero}} = 27$ mag). The resulting 2-D star models per band are shown in the third row of Fig. 11, and the fitted star magnitudes are indicated in the titles of each column. In the fourth panel, we present the residuals obtained by subtracting the models from the observations, revealing

⁴ <https://github.com/ICRAR/ProFit>

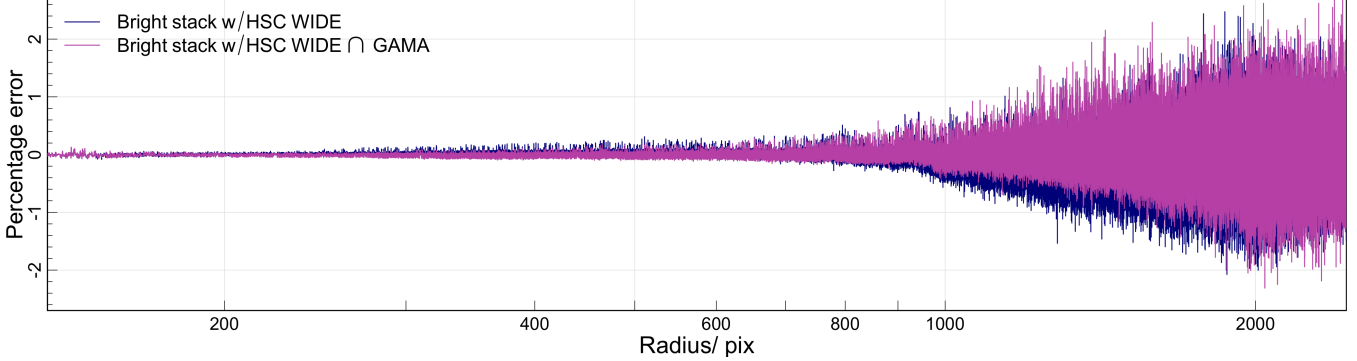


Figure 9. The pink percentage error curve shows the difference between the data from the outer stack created with the $m_g < 8$ from HSC Wide \cap GAMA and a model created with this data. Instead, the blue curve shows the percentage error between the data of the outer stack with all $m_g < 8$ stars from HSC Wide and the model mentioned above. By comparing both outer parts of the PSF profiles, we find no significant differences between them, and this way we verify that stacking more bright stars does not improve the resulting PSFs.

some residuals around the core of the stars. However, when we plot the subtracted images divided by the corresponding ProFit model (see fifth row), we see that the percentage difference is very low around the central regions. Finally, in the sixth row, we show the 1-D radial profile of the star up to a radius of $R \sim 1500$ pixels in light blue, the masked star profile in dark blue, and the ProFit model profile in red. The dashed black lines indicate the radii where the core of each star is saturated. We observe that the point-source models that were constructed with our empirical HSC-SSP PDR3 PSF images reproduce well the data across all five filters, including the vertical spikes in the Y -band star image. We also see that the noise of the ProFit models is reduced compared to the noise of the star images as a consequence of the PSF stacking technique reconstruction.

5.2 Galaxy group application

Our goal in this application is to make an estimation of how much of the total light of a galaxy group is actually in the intra-halo light component (i.e. the fraction of IHL or f_{IHL}). As the IHL is a faint component, the PSF-scattered flux could have a major impact on its measurement. We compensate for the PSF effect by estimating how much flux is spread, reallocating the lost flux to every source, and removing the PSF-scattered light from the original group image. Building on this innovative PSF removal technique, we make a more realistic IHL estimation.

5.2.1 PSF-scattered light removal

We use the HSC-SSP PDR3 PSFs to remove the scattered light from a group image of 14 galaxies located in the HSC UD SXDS field. We use the GAMA galaxy group catalogue G^3Cv10 to select the group, which has GAMA GroupID = 400020, halo mass $M_{\text{halo}} = 8.7 \cdot 10^{13} h^{-1} M_\odot$, virial radius $R_{\text{vir}} = 765$ kpc, and redshift $z = 0.258$. For the purpose of this selection, we chose between groups with more than 10 members (G^3Cv10 mass estimations are robust when $N > 10$) and we discard the groups that have bright stars within 5 arcmin from the BGG. In Fig. 12 we present a 6.5 arcmin² color composite image of the selected group, made with the HSC g,i,Y -filters, where the brightest group galaxy (BGG) of the system is located at the centre of the image and the pink circles are indicating the centres of each spectroscopically confirmed group member. However, we make our IHL estimations on a smaller region of 2.8 arcmin² in order to avoid

the two bright stars located in the north of the field, and therefore only 10 out of the 14 members are being considered in this cutout.

The process we follow to remove the PSF-scattered light from the 2.8 arcmin² galaxy group image is explained in detail here:

- (i) subtract the median sky value from the group image;
- (ii) run PROFOUND in the source detection mode. PROFOUND identifies the objects in the image, creates segmentation maps around every detected source, and determines a flux estimation for each one;
- (iii) reset all pixel values outside the segmentation maps (what we call "sky") to zero;
- (iv) to reproduce the PSF effect, convolve the image with sky = 0 (we ensure the spread light comes purely from the sources) with the PSF via the fast Fourier transform (FFT) technique by making use of the `profitMakeConvolver` and `profitConvolve`⁵ functions;
- (v) to quantify the spread effect, count the flux inside each segment before ($\text{Flux}_{\text{meas}}$) and after the convolution ($\text{Flux}_{\text{conv}}$). This gives us a factor $C = \text{Flux}_{\text{meas}} / \text{Flux}_{\text{conv}}$;
- (vi) to ensure the conservation of the flux, rescale the measured flux of each segment by doing $\text{Flux}_{\text{real}} = \text{Flux}_{\text{meas}} \cdot C$ in the image with sky=0, where $\text{Flux}_{\text{real}}$ is the real flux after compensating for the PSF-scattered light. This image (Output 1) contains only $\text{Flux}_{\text{real}}$ (unaffected by the PSF) from the galaxy group;
- (vii) convolve Output 1 with the HSC-SSP PDR3 PSF;
- (viii) mask the resulting PSF-convolved image and subtract it from the masked original group image. This image (Output 2) contains only the PSF-subtracted IHL flux.

In Fig. 13 we show a schematic overview of the processing steps mentioned above to remove the PSF scattered light from a group image. In our case, the analysis is focused on estimating the IHL of the galaxy group only in the HSC r -filter. Both g and r -bands achieve very similar effective depths, but due to the cosmically cleaner images, we use the r -band for this initial application. We also note the scatter in the mass-to-light ratio is smaller in the r -band (see Robotham et al. 2020), suggesting this filter is the most likely to provide a better approximation of the IHL stellar light fraction.

In (i), the median sky value in the r -band image of our group is $\text{sky}_r = 0.0005$. After running PROFOUND, setting the sky to 0 in (iii)

⁵ ProFit functions: `profitMakeConvolver` creates the convolver object given the PSF and convolution technique, and `profitConvolve` performs the convolution given the image, PSF, and convolver object.

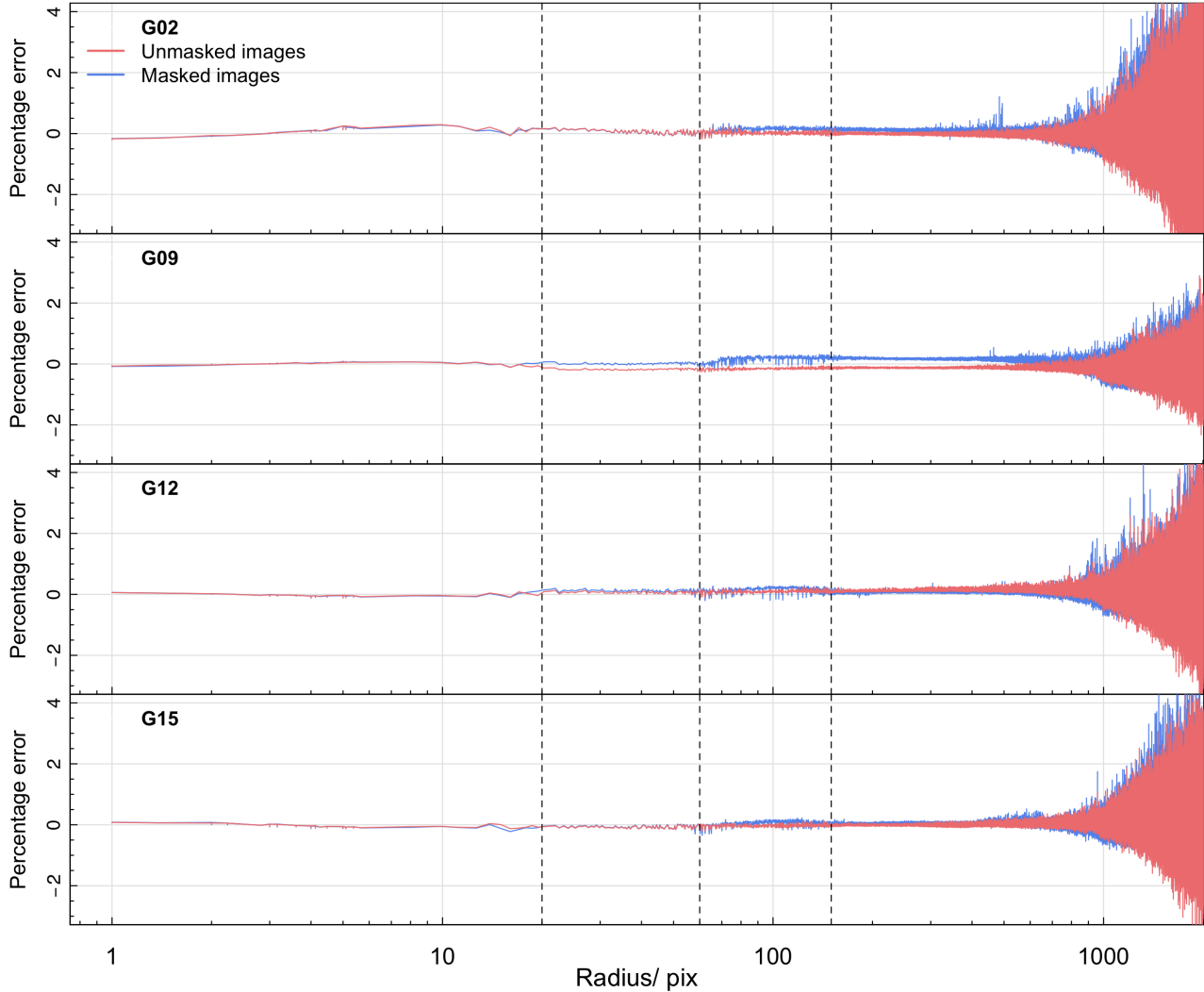


Figure 10. Difference between a PSF image constructed by stacking the unmasked star images versus stacking the masked star images expressed by percentage errors per GAMA field. The salmon curve shows the difference between the unmasked PSF data and the final PSF model, where the final PSF is the result of stacking the PSFs from each GAMA field generated with the unmasking technique. Instead, the blue curve shows the difference between the unmasked PSF image and the same final PSF model. The relative difference is noisier when using the masking technique, meaning that stacking unmasked star images leads to a better S/N in the final PSF. The *g*-band represents the optimum case, as in the other bands the percentage errors go up to 4%.

is a key step to estimate how much flux is lost outside the segments as a consequence of the PSF convolution. Without setting $\text{sky} = 0$, the scattered light from the sky could get inside the segments, resulting in an inaccurate estimation of the PSF effect. To convolve, we use the *r*-band HSC-SSP PDR3 PSF model, both (iv) and (vii) convolutions take ~ 4 sec. Although the observed group image is already affected by the PSF, we only use the (iv) convolution to get an estimation of the percentage of flux spread within every segment. Each segment has this information saved in the factor C . By doing $\text{Flux}_{\text{real}} = \text{Flux}_{\text{meas}} \cdot C$, we transform the measured flux of every source to the real flux unaffected by the PSF. Output 1 has only the flux from the galaxy members with $\text{Flux}_{\text{real}}$, where this image is used to estimate the SB profiles of the group. However, the scattered flux outside the segments is still physically present in the image. To remove it, we simulate again the PSF effect by convolving Output 1 with the PSF in (vii). As the $\text{sky}=0$ in Output 1, the scattered

flux in (6) outside the segments comes purely from the sources. We then mask the resulting image (6) and the original image (1). In the last step (viii), we subtract masked (6) from masked (1), where the remaining flux is the IHL of the group after removing the PSF flux. We use this image to estimate the SB profiles of the IHL.

5.2.2 IHL estimation

Figure 14 shows the surface brightness profiles measured from the original imaging (green profiles) versus the profiles from the image where we subtract the PSF-scattered light (orange profiles). To calculate these SB profiles we estimate the median surface brightness within consecutive circular annular apertures. The radial range of these apertures goes from $R = 0$ to $R \sim 330$ kpc, divided into 50 equally linearly distributed bins. Each annulus within these bins has a width of 10 pixels. The solid lines present the galaxies plus IHL flux,

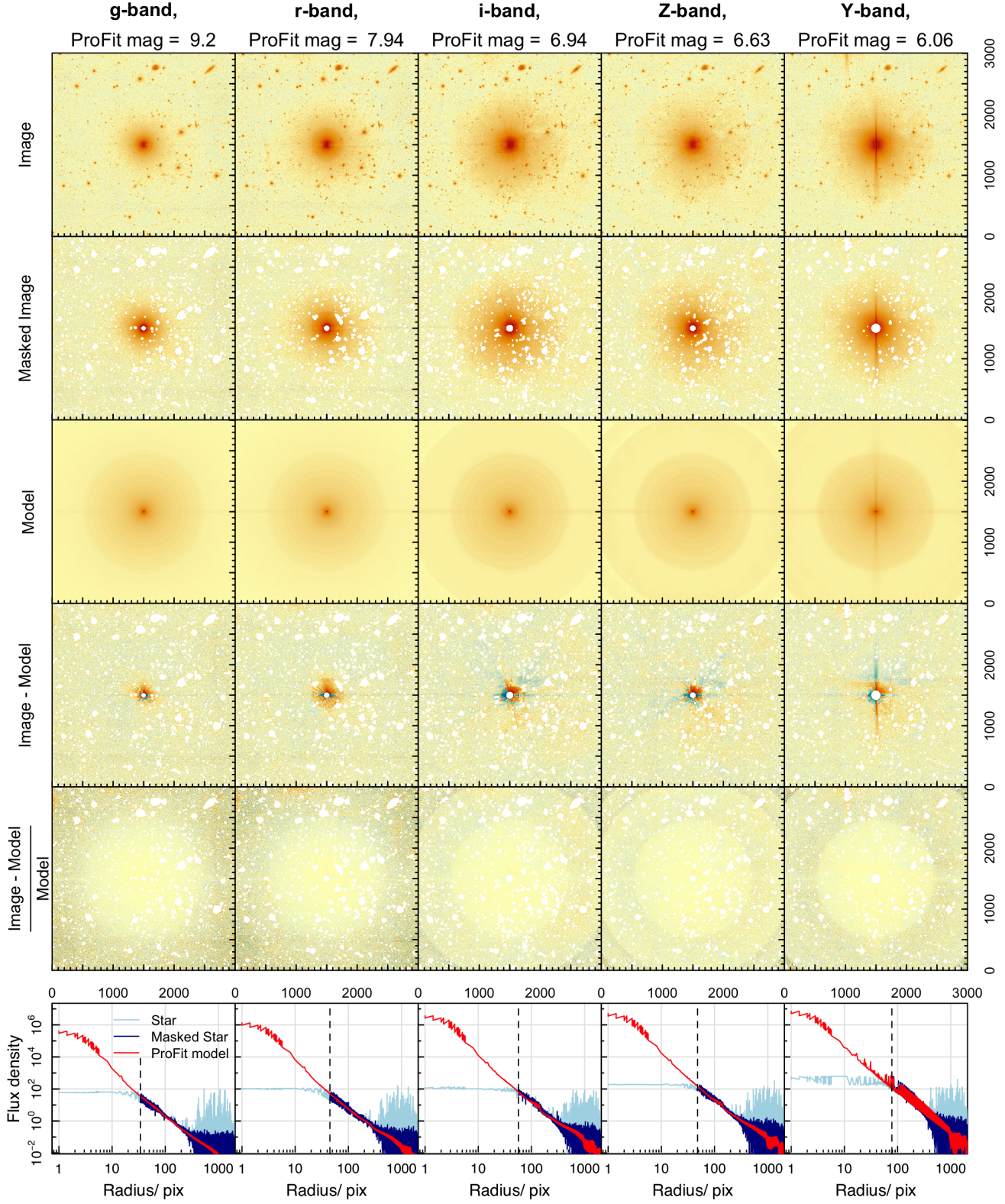


Figure 11. HSC-SSP PDR3 PSF application to model a real HSC star image located in G09, where each column represents each of the HSC g,r,i,Z,Y filters. The first row shows the image of the star up to an extent of $R \sim 3000$ pix. The second row shows the masked version of the star image. The third row shows the ProFit model of the star, where we are making use of our HSC PSFs. The resulting fitted magnitudes per band are indicated in the headings of each column. In the next row, we show the result of subtracting the star ProFit model from the masked star image (2nd row - 3rd row). The fifth row shows the subtraction of the masked image from the star model divided by the star model. The bottom panels show the 1-D radial profile of the star in light blue, the profile of the masked version of the star in dark blue, and the profile of the ProFit star model in red. The dashed black line indicates the radius up to where we mask the core of the star.

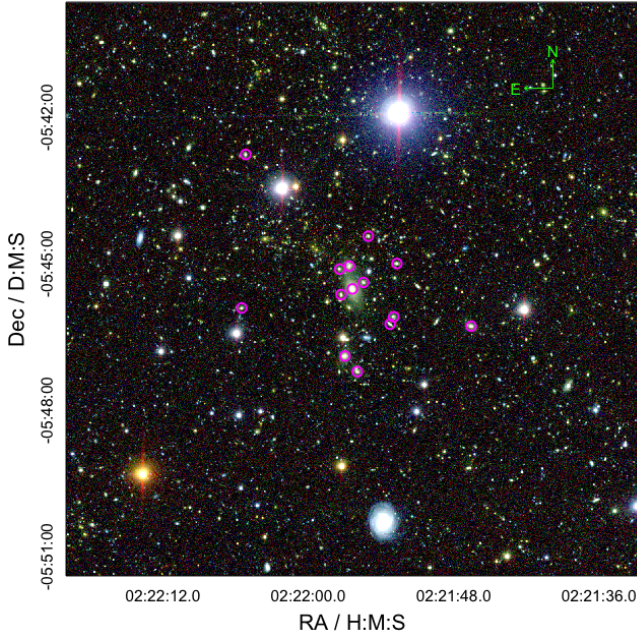


Figure 12. RGB image of the selected HSC UD SXDS group of galaxies for our HSC-SSP PDR3 PSFs analysis, centred on the BCG of the system. The centers of each of the 14 galaxy group members are indicated with pink circles. This GAMA group is identified by the ID 400020 on the G³Cv10 group catalogue, with a halo mass of $M_{\text{halo}} = 8.7 \cdot 10^{13} h^{-1} M_{\odot}$ and a redshift of $z = 0.258$. The image size is 6.5 arcmin.

whereas the dashed lines are the SB profiles when we only consider the IHL component. To generate Group+IHL profiles, we generate them separately from Output 1 (which contains only the flux from the group) and Output 2 (which contains only the flux from the IHL). The pale lines come from the Group+IHL profiles when different values are taken in the sky subtraction step. This range goes from 0.0002 to 0.0013, where the dark green and orange profiles are made with a mean sky subtraction value of $\text{sky}_r = 0.0005$. All profiles are in the observed reference frame, except for the brown and blue lines, which are the SB profiles when accounted for the SB dimming in the form $(1+z)^{-4}$ (Tolman 1930).

We then measure the r -band IHL fraction of the group in the observed reference frame using these processed images. This is computed by summing all the IHL flux within a circle of radius R centered on the BGG divided by the total flux produced by the members of the group (inside the 2.8 arcmin² region) and the IHL (Group+IHL), also contained in the same circle of radius R . The profile of the f_{IHL}^r as a function of the radius of the circular aperture is shown in the bottom panel of Figure 15, where the orange dashed line indicates the f_{IHL}^r when removing the PSF-scattered light and the green solid line indicates the f_{IHL}^r from the original image. The upper panel is a zoom-in region of $2.8 \times 2.8 \text{ arcsec}^2$ over the group after removing the PSF light and masking all the sources, where the 200 kpc circular aperture is indicated by the black dashed circle and the members of the group by black crosses.

We also show the distribution of IHL surface brightness by plotting the cumulative density distribution (CDF) in Fig. 16. The CDF of the Group+IHL is in the left panel with solid lines and the single IHL component is on the right panel with dashed lines. The orange CDFs are from the PSF-subtracted images and the green CDFs are from the original images.

5.2.3 Implications for IHL measurements

In Figure 14, the orange curves are fainter than the green curves in the outskirts due to the removal of PSF-scattered light. It is clear that at very low SB, the profiles are highly dependent on the selected sky subtraction value, meaning that the profile errors are dominated by our subtraction choices. We can see how the scattered light caused by the PSF overestimates the flux measurements when $R > 90$ kpc up to a difference of almost $\sim 2 \text{ mag arcsec}^{-2}$.

In Figure 15, the percentage of flux in the IHL component ranges from $\sim 5\%$ at 60 kpc to $\sim 20\%$ at 240 kpc. Specifically, the f_{IHL}^r is overestimated by $\sim 30\%$ at $R = 200$ kpc (black dashed vertical line) when we do not remove the scattered light of the PSF.

In Figure 16, the Group+IHL SB pixel values range between 28 and $19 \text{ mag arcsec}^{-2}$, whereas the SB pixels of the IHL component range between 28 and $25 \text{ mag arcsec}^{-2}$. In the right panel, we can see how the fraction of pixels fainter than a certain surface brightness limit (SBL) is higher for the IHL-PSF subtracted CDF, which agrees with our previous findings in Figures 14 and 15.

The most commonly used technique in the literature to separate the BGG from the IHL is to use an SBL or SB cut, which assumes that all the light below this limit is IHL. The widely adopted SBL in the V -band is $\mu_V^{\text{lim}} = 26 \text{ mag arcsec}^{-2}$ (Feldmeier et al. 2002, 2004; Mihos et al. 2005; Rudick et al. 2006, 2009, 2010, 2011). In the r -band, a SBL of $\mu_r^{\text{lim}} = 26.4 \text{ mag arcsec}^{-2}$ has been used in the literature (Krick & Bernstein 2007). The vertical dashed black lines in both panels of Figure 16 indicate the SBL $\mu_r^{\text{lim}} = 26.4 \text{ mag arcsec}^{-2}$. When applying this SB cut method on the left panel, only $\sim 11\%$ of the Group+IHL pixels are fainter than μ_r^{lim} . This result is nearly independent of the PSF subtraction. However, when we analyse this SBL in the right panel of Fig. 16 (black dashed horizontal lines), we can appreciate that the fraction of IHL pixels fainter than $\mu_r^{\text{lim}} = 26.4 \text{ mag arcsec}^{-2}$ is ~ 0.45 for the green profile and ~ 0.54 in the IHL PSF subtracted scenario. This means that approximately half of the light would not be considered as IHL according to the SB cut technique, whereas following our methodology we find IHL flux up to an SB of $\mu_r \sim 25 \text{ mag arcsec}^{-2}$.

6 CONCLUSIONS

In this paper, we make public our new HSC-SSP PDR3 empirical PSF models for all g,r,i,Z,Y HSC filters. Using stacks of star images within a wide brightness range and following the method outlined by Infante-Sainz et al. (2020), we characterise the PSFs up to an extent of $R \sim 5.6$ arcmin. These extended models have a significant impact on the study of low surface brightness structures and will assist the HSC community in recovering the spread light from point and extended sources, as well as removing the contaminating light at large angles.

By comparing the PSF models from the different GAMA regions, we verify that the HSC PDR3 PSFs are stable across space and time. We then prove that our sophisticated median stacking technique with the unmasked background sources shows better results compared to the commonly used median stacking method of masking all background sources. Finally, we also demonstrate that increasing the number of stacked star images does not lead to better PSFs in terms of S/N at large radii.

We present two examples showing the performance of our PSFs in scientific applications. In the first application, we use the HSC PDR3 PSFs to fit a 2-D model of a star image in each filter. We demonstrate that our PSF models effectively make a good characterisation of

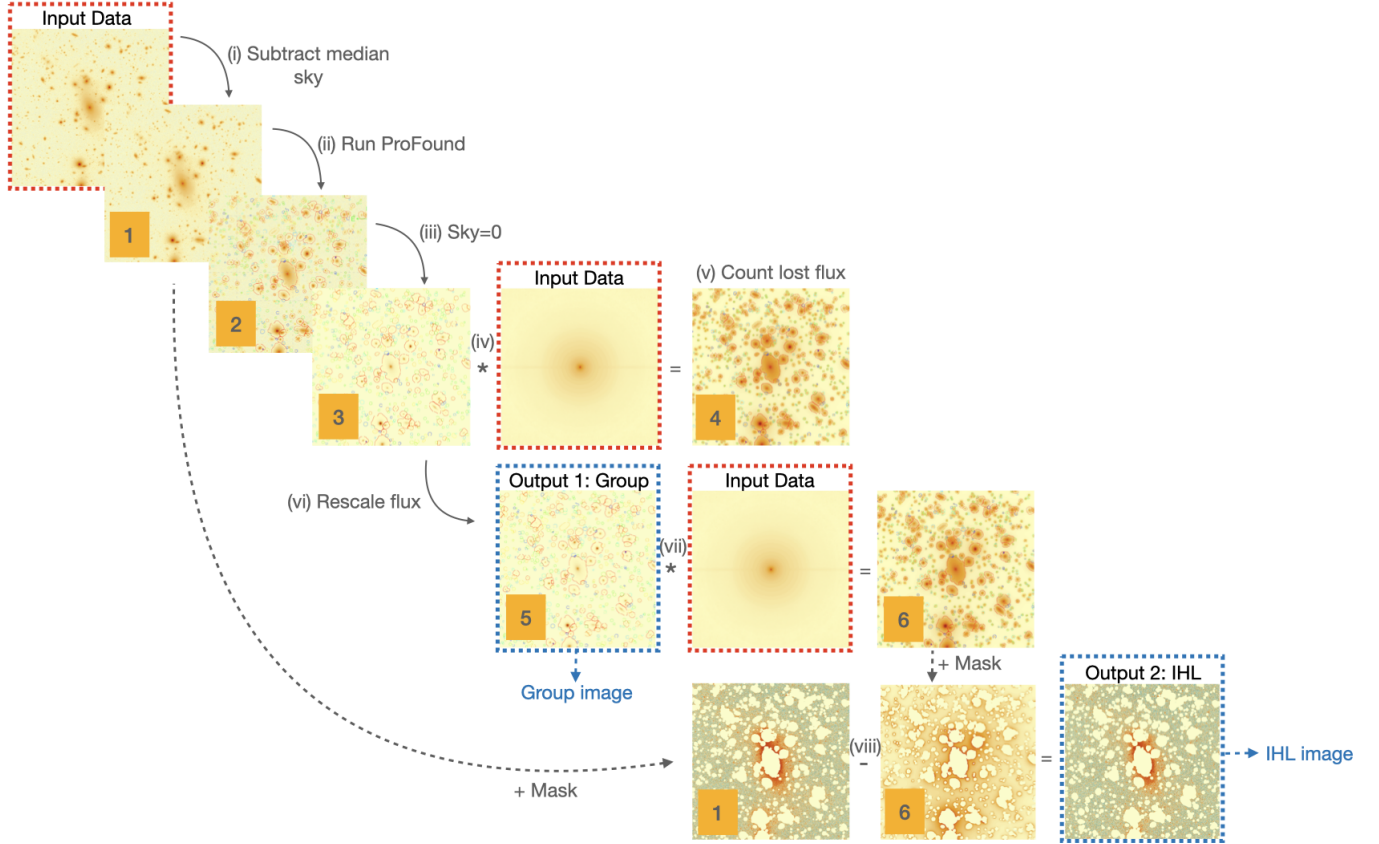


Figure 13. Schematic view of the processing steps outlined in Sec. 5.2 to remove the PSF scattered light from the group image. All the panels (except for the PSF) are images of a zoom-in region of $2.8 \times 2.8 \text{ arcsec}^2$ in the r -band, centred at the BCG of the 400020 GAMA group. The sources identified by ProFound in (ii) are delimited by multi-colored segments.

these star images. In the second application, we select a group of 14 galaxies from the GAMA galaxy group catalogue G³Cv10 located in the HSC UD SXDS field to analyse the IHL component in the r -band (GAMA GroupID = 400020, $M_h = 8.7 \cdot 10^{13} \text{ h}^{-1} M_\odot$, $z = 0.258$). Using advanced source extraction techniques, we measure the surface brightness profiles for both the Group+IHL and the single IHL component up to $R \sim 300 \text{ kpc}$ and $\text{SB} \sim 31 \text{ mag arcsec}^{-2}$. We show that IHL can be overestimated by almost 2 mag in the original group image. Following this approach, we estimate the IHL fraction radial profile of 400020. The results show a median f_{IHL}^r of ~ 0.13 , which is found to be overestimated by $\sim 30\%$ when the PSF-scattered light is not removed. In addition, we find that the widely used SB cut of $\mu_r^{\text{lim}} = 26.4 \text{ mag arcsec}^{-2}$ to separate the IHL component from the galaxy profile can underestimate the f_{IHL}^r by a factor of two. This result is independent of the PSF subtraction. We compare the f_{IHL}^r and IHL SB values with and without the removal of the PSF-spread light in Table 3.

The 2-D HSC PDR3 PSFs models are available as FITS files at https://github.com/luciagarate/HSC_PSFs, as well as the scripts to reproduce the reconstruction process.

ACKNOWLEDGEMENTS

LPGN, ASGR, and SB acknowledge support from the ARC Future Fellowship scheme (FT200100375). LJMD acknowledges support from the ARC Future Fellowship scheme (FT200100055).

This paper is based on data collected at the Subaru Telescope and retrieved from the HSC data archive system, which is operated by the Subaru Telescope and Astronomy Data Center (ADC) at NAOJ. Data analysis was in part carried out with the cooperation of Center for Computational Astrophysics (CfCA), NAOJ. We are honored and grateful for the opportunity of observing the Universe from Maunakea, which has the cultural, historical, and natural significance in Hawaii. The Hyper Suprime-Cam (HSC) collaboration includes the astronomical communities of Japan and Taiwan, and Princeton University. The HSC instrumentation and software were developed by the National Astronomical Observatory of Japan (NAOJ), the Kavli Institute for the Physics and Mathematics of the Universe (Kavli IPMU), the University of Tokyo, the High Energy Accelerator Research Organization (KEK), the Academia Sinica Institute for Astronomy and Astrophysics in Taiwan (ASIAA), and Princeton University. Funding was contributed by the FIRST program from the Japanese Cabinet Office, the Ministry of Education, Culture, Sports, Science and Technology (MEXT), the Japan Society for the Promotion of Science (JSPS), Japan Science and Technology Agency (JST), the Toray Science Foundation, NAOJ, Kavli IPMU, KEK, ASIAA, and Princeton University. This paper makes use of software developed for the Large Synoptic Survey Telescope. We thank the LSST Project for making their code available as free software at <http://dm.lsst.org>.

We have used catalogues from GAMA, a joint European-Australasian project based around a spectroscopic campaign using the Anglo-Australian Telescope. The GAMA input catalogue

f_{IHL}^r	Without PSF subtraction	With PSF subtraction
100 kpc	0.15	0.12
150 kpc	0.16	0.13
200 kpc	0.18	0.14
IHL SB/ mag arcsec⁻² (observed)		
100 kpc	27.2	27.5
150 kpc	28.1	28.6
200 kpc	29.3	31
IHL SB/ mag arcsec⁻² (dimming corrected)		
100 kpc	26.2	26.5
150 kpc	27.1	27.6
200 kpc	28.3	30

Table 3. Fraction of IHL in the *r*-band when removing the PSF-spread light versus when we do not remove it at 100, 150, and 200 kpc from the BCG of the 400020 GAMA group. We additionally show the IHL SB values estimations.

is based on data taken from the Sloan Digital Sky Survey and the UKIRT Infrared Deep Sky Survey. Complementary imaging of the GAMA regions is being obtained by a number of independent survey programmes including GALEX MIS, VST KiDS, VISTA VIKING, WISE, Herschel-ATLAS, GMRT and ASKAP providing UV to radio coverage. GAMA is funded by the STFC (UK), the ARC (Australia), the AAO, and the participating institutions. The GAMA website is <http://www.gama-survey.org/>.

All of the work presented here was made possible by the free and open R software environment ([R Core Team 2023](#)). All figures in this paper were made using the R MAGICAXIS package ([Robotham 2016b](#)). This work also makes use of the CELESTIAL package ([Robotham 2016a](#)).

DATA AVAILABILITY

The HSC-SSP PDR3 PSFs FITS files and reconstruction scripts are available at https://github.com/luciagarate/HSC_PSFs. The images are from the Hyper Suprime-Cam Public Data Release 3 (HSC-PDR3; [Aihara et al. 2022](#)) and can be obtained from https://hsc-release.mtk.nao.ac.jp/doc/index.php/data-access_pdr3/. The catalogue information was extracted from the Galaxy And Mass Assembly (GAMA) survey Galaxy Group Catalogue (G³Cv10; [Robotham et al. 2011](#)).

REFERENCES

- Abraham R. G., van Dokkum P. G., 2014, *PASP*, **126**, 55
 Aihara H., et al., 2018, *PASJ*, **70**, S8
 Aihara H., et al., 2019, *PASJ*, **71**, 114
 Aihara H., et al., 2022, *PASJ*, **74**, 247
 Baldry I. K., et al., 2010, *MNRAS*, **404**, 86
 Beckwith S. V. W., et al., 2006, *AJ*, **132**, 1729
 Bernstein R. A., 2007, *ApJ*, **666**, 663
 Bertin E., 2013, PSFEx: Point Spread Function Extractor, *Astrophysics Source Code Library*, record ascl:1301.001 (ascl:1301.001)
 Born M., Wolf E., 1999, Principles of Optics. Cambridge University Press;
 7th edition
 Bosch J., et al., 2018, *PASJ*, **70**, S5
 Bosch J., et al., 2019, in Teuben P. J., Pound M. W., Thomas B. A., Warner E. M., eds, Astronomical Society of the Pacific Conference Series Vol. 523, Astronomical Data Analysis Software and Systems XXVII. p. 521 ([arXiv:1812.03248](#)), doi:10.48550/arXiv.1812.03248
 Bower R. G., Benson A. J., Malbon R., Helly J. C., Frenk C. S., Baugh C. M., Cole S., Lacey C. G., 2006, *MNRAS*, **370**, 645
 Cohen Y., et al., 2018, *ApJ*, **868**, 96
 D'Souza R., Kauffmann G., Wang J., Vegetti S., 2014, *MNRAS*, **443**, 1433
 Davis M., et al., 2007, *ApJ*, **660**, L1
 Driver S. P., et al., 2011, *MNRAS*, **413**, 971
 Driver S. P., et al., 2022, *MNRAS*, **513**, 439
 Feldmeier J. J., Mihos J. C., Morrison H. L., Rodney S. A., Harding P., 2002, *ApJ*, **575**, 779
 Feldmeier J. J., Ciardullo R., Jacoby G. H., Durrell P. R., 2004, *ApJ*, **615**, 196
 Fliri J., Trujillo I., 2016, *MNRAS*, **456**, 1359
 Furnell K. E., et al., 2021, *MNRAS*, **502**, 2419
 Furusawa H., et al., 2008, *ApJS*, **176**, 1
 Gaia Collaboration et al., 2022, arXiv e-prints, p. [arXiv:2208.00211](#)
 Gallagher John S. I., Ostriker J. P., 1972, *AJ*, **77**, 288
 Gonzalez A. H., Zabludoff A. I., Zaritsky D., 2005, *ApJ*, **618**, 195
 Greco J. P., et al., 2018a, *ApJ*, **857**, 104
 Greco J. P., Goulding A. D., Greene J. E., Strauss M. A., Huang S., Kim J. H., Komiyama Y., 2018b, *ApJ*, **866**, 112
 Infante-Sainz R., Trujillo I., Román J., 2020, *MNRAS*, **491**, 5317
 Janowiecki S., Mihos J. C., Harding P., Feldmeier J. J., Rudick C., Morrison H., 2010, *ApJ*, **715**, 972
 Kado-Fong E., et al., 2021, *ApJ*, **920**, 72
 Kawanomoto S., et al., 2018, *PASJ*, **70**, 66
 Kelvin L. S., Hasan I., Tyson J. A., 2023, *MNRAS*, **520**, 2484
 King I. R., 1971, *PASP*, **83**, 199
 Kolmogorov A., 1941, Akademiia Nauk SSSR Doklady, **30**, 301
 Komiyama Y., et al., 2018, *PASJ*, **70**, S2
 Kriss J. E., Bernstein R. A., 2007, *AJ*, **134**, 466
 Krist J., 1995, in Shaw R. A., Payne H. E., Hayes J. J. E., eds, Astronomical Society of the Pacific Conference Series Vol. 77, Astronomical Data Analysis Software and Systems IV. p. 349
 LSST Science Collaboration et al., 2009, arXiv e-prints, p. [arXiv:0912.0201](#)
 La Barbera F., Ferreras I., de Carvalho R. R., Bruzual G., Charlot S., Pasquali A., Merlin E., 2012, *MNRAS*, **426**, 2300
 Liske J., et al., 2015, *MNRAS*, **452**, 2087
 Liu Q., et al., 2023, *ApJ*, **953**, 7
 Mandelbaum R., Hyper Suprime-Cam (HSC) Collaboration 2017, in American Astronomical Society Meeting Abstracts #229. p. 226.02

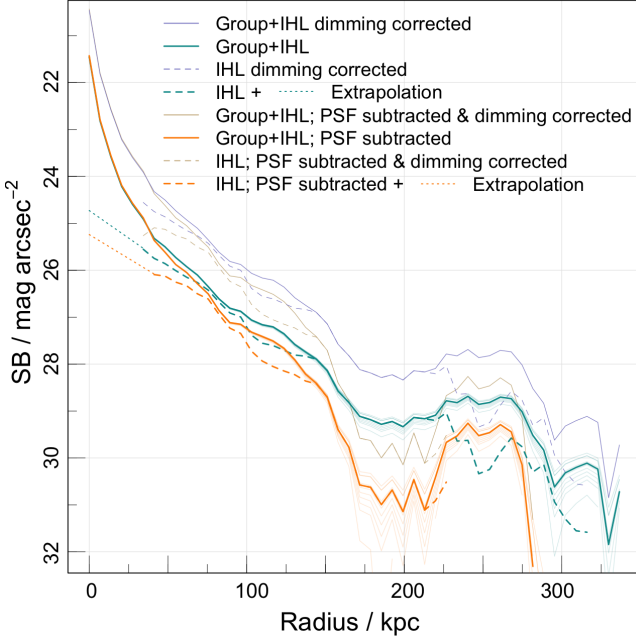


Figure 14. Observed surface brightness profiles of the original group image (green color) versus the PSF-subtracted image (orange color). In both cases, the Group+IHL SB profiles are plotted with solid lines, whereas the SB profiles of the single IHL components are plotted with dashed lines. We extrapolate both IHL profiles with dotted lines to account for the lost flux caused by the masking of the BGG. The solid pale lines are the Group+IHL profiles created with different sky subtraction values, going from 0.0002 to 0.0013. The dark solid profiles are made with the median sky subtraction value: 0.00055. Additionally, we show the SB profiles when corrected for the surface brightness dimming with blue (not PSF-subtracted) and brown (PSF-subtracted) lines. Magnitudes are in the AB magnitude system and the HSC-SSP PDR3 zero point is $m_{\text{zero}} = 27$ mag.

- Martínez-Lombilla C., Knapen J. H., 2019, *A&A*, **629**, A12
 Martínez-Lombilla C., et al., 2023, *MNRAS*, **518**, 1195
 Merritt D., 1984, *ApJ*, **276**, 26
 Merritt A., van Dokkum P., Abraham R., Zhang J., 2016a, *ApJ*, **830**, 62
 Merritt A., van Dokkum P., Danieli S., Abraham R., Zhang J., Karachentsev I. D., Makarova L. N., 2016b, *ApJ*, **833**, 168
 Merritt A., Pillepich A., van Dokkum P., Nelson D., Hernquist L., Marinacci F., Vogelsberger M., 2020, *MNRAS*, **495**, 4570
 Mihos J. C., Harding P., Feldmeier J., Morrison H., 2005, *ApJ*, **631**, L41
 Mihos J. C., Janowiecki S., Feldmeier J. J., Harding P., Morrison H., 2009, *ApJ*, **698**, 1879
 Mihos J. C., Harding P., Feldmeier J. J., Rudick C., Janowiecki S., Morrison H., Slater C., Watkins A., 2017, *ApJ*, **834**, 16
 Miyazaki S., et al., 2015, *ApJ*, **807**, 22
 Miyazaki S., et al., 2018, *PASJ*, **70**, S1
 Moffat A. F. J., 1969, *A&A*, **3**, 455
 Montes M., 2022, *Nature Astronomy*, **6**, 308
 Montes M., Brough S., Owers M. S., Santucci G., 2021, *ApJ*, **910**, 45
 Murante G., et al., 2004, *ApJ*, **607**, L83
 Nelson P. G., Tomczyk S., Elmore D. F., Kolinski D. J., 2008, in Stepp L. M., Gilmozzi R., eds, Society of Photo-Optical Instrumentation Engineers (SPIE) Conference Series Vol. 7012, Ground-based and Airborne Telescopes II. p. 701231, doi:10.1117/12.789494
 Newman J. A., et al., 2013, *ApJS*, **208**, 5
 Oliver S., et al., 2000, *MNRAS*, **316**, 749
 Pierre M., et al., 2004, *J. Cosmology Astropart. Phys.*, **2004**, 011
 Planck Collaboration et al., 2020, *A&A*, **641**, A6
 R Core Team 2023, R: A Language and Environment for Statistical Computing. R Foundation for Statistical Computing, Vienna, Austria, <https://www.R-project.org/>

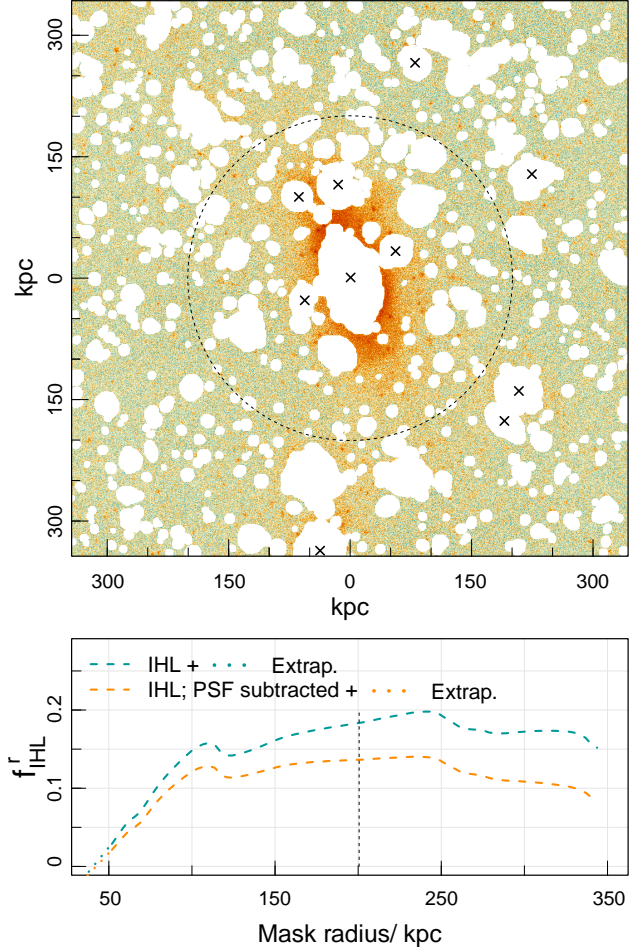


Figure 15. The upper panel is the 2.8×2.8 arcsec 2 r -band group image when subtracting the PSF-convolved image from the original one and masking all the sources (final image in Fig. 13). The lower panel indicates the fraction of IHL in the r -band as a function of the radius of the circular aperture where we estimate the f_{IHL}^r . The green dashed line shows the f_{IHL}^r of the original image, whereas the orange dashed line shows the profile of the PSF-subtracted image. The dotted lines are the extrapolated profiles to account for the IHL lost flux caused by the masking of the BGG. At $R = 200$ kpc (marked by the black dashed vertical line in the bottom panel and by the black dashed circle in the upper one), the estimated value of f_{IHL}^r is found to be overestimated by approximately 30% when the scattered light from the PSF is not removed.

- //www.R-project.org/
 Racine R., 1996, *PASP*, **108**, 699
 Robotham A. S. G., 2016a, Celestial: Common astronomical conversion routines and functions, Astrophysics Source Code Library, record ascl:1602.011 (ascl:1602.011)
 Robotham A. S. G., 2016b, magicaxis: Pretty scientific plotting with minor-tick and log minor-tick support, Astrophysics Source Code Library, record ascl:1604.004 (ascl:1604.004)
 Robotham A., et al., 2010, *Publ. Astron. Soc. Australia*, **27**, 76
 Robotham A. S. G., et al., 2011, *MNRAS*, **416**, 2640
 Robotham A. S. G., Taranu D. S., Tobar R., Moffett A., Driver S. P., 2017, *MNRAS*, **466**, 1513
 Robotham A. S. G., Davies L. J. M., Driver S. P., Koushan S., Taranu D. S., Casura S., Liske J., 2018, *MNRAS*, **476**, 3137
 Robotham A. S. G., Bellstedt S., Lagos C. d. P., Thorne J. E., Davies L. J., Driver S. P., Bravo M., 2020, *MNRAS*, **495**, 905
 Rudick C. S., Mihos J. C., McBride C., 2006, *ApJ*, **648**, 936
 Rudick C. S., Mihos J. C., Frey L. H., McBride C. K., 2009, *ApJ*, **699**, 1518

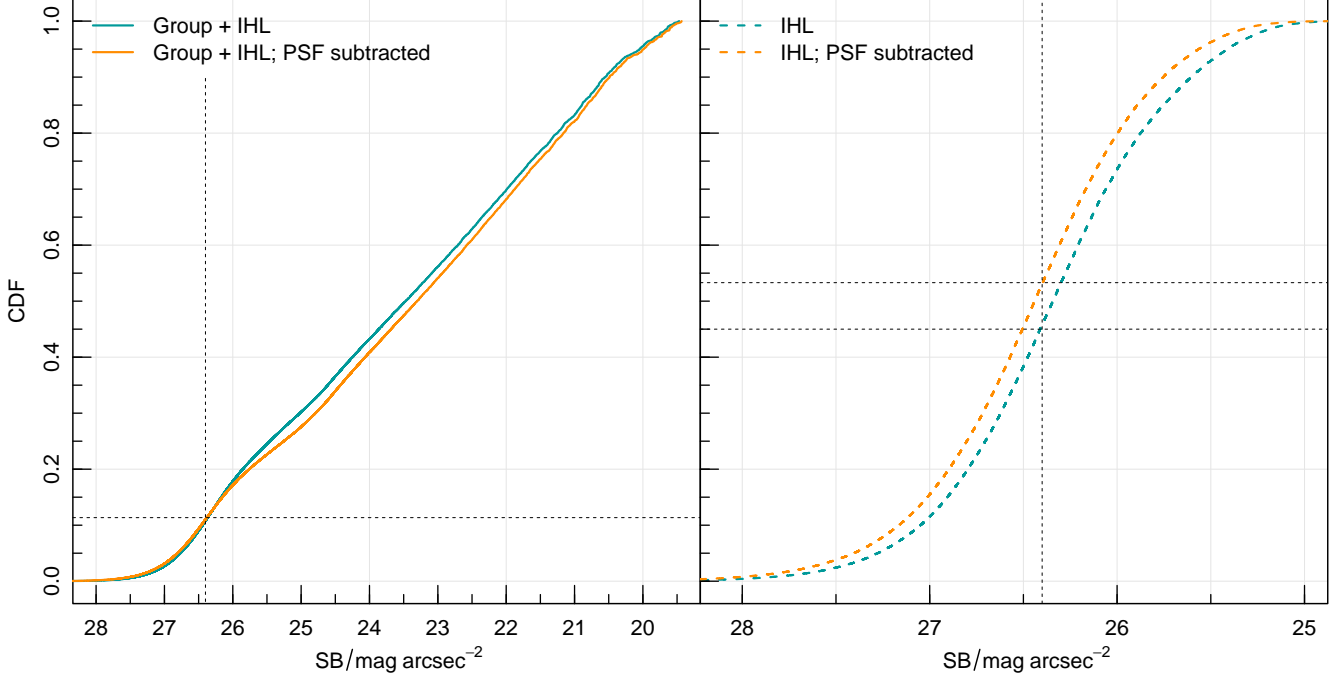


Figure 16. Surface brightness cumulative density distributions of the Group+IHL (left panel, solid lines) and the IHL single component (right panel, dashed lines). In both panels, the green lines are the CDFs of the original image, whereas the orange lines are the CDFs of the PSF-subtracted image. The vertical dashed black lines indicate the commonly used r -band IHL SBL in the SB cut method: $\mu_r^{\lim} = 26.4 \text{ mag arcsec}^{-2}$. The f_{IHL}^r is underestimated by a factor of two according to this technique.

- Rudick C. S., Mihos J. C., Harding P., Feldmeier J. J., Janowiecki S., Morrison H. L., 2010, *ApJ*, **720**, 569
 Rudick C. S., Mihos J. C., McBride C. K., 2011, *ApJ*, **732**, 48
 Sandin C., 2014, *A&A*, **567**, A97
 Scoville N., 2007, in Baker A. J., Glenn J., Harris A. I., Mangum J. G., Yun M. S., eds, Astronomical Society of the Pacific Conference Series Vol. 375, From Z-Machines to ALMA: (Sub)Millimeter Spectroscopy of Galaxies. p. 166
 Slater C. T., Harding P., Mihos J. C., 2009, *PASP*, **121**, 1267
 Springel V., et al., 2005, *Nature*, **435**, 629
 Tang L., Lin W., Cui W., Kang X., Wang Y., Contini E., Yu Y., 2018, *ApJ*, **859**, 85
 Tolman R. C., 1930, *Proceedings of the National Academy of Science*, **16**, 511
 Trujillo I., Bakos J., 2013, *MNRAS*, **431**, 1121
 Trujillo I., Fliri J., 2016, *ApJ*, **823**, 123
 Uson J. M., Boughn S. P., Kuhn J. R., 1991, *ApJ*, **369**, 46
 York D. G., et al., 2000, *AJ*, **120**, 1579
 de Jong R. S., 2008, *MNRAS*, **388**, 1521
 de Vaucouleurs G., 1948, *Annales d'astrophysique*, **11**, 247
 de Vaucouleurs G., 1953, *MNRAS*, **113**, 134
 de Vaucouleurs G., 1958, *ApJ*, **128**, 465

APPENDIX A: HSC-SSP PDR3 PSFS IN THE RESTING BANDS

In Sec. 4.1 we discuss the temporal and spatial stability of the HSC-SSP PDR3 PSF across the different GAMA regions in the g -band case. Fig. A1 shows the HSC PSFs in all the filters, where, once again, we see no major differences between the different regions.

In Fig. A2, we present the HSC-SSP PDR3 g, r, i, Z, Y -band PSFs up to an extent of $R \sim 5.6$ arcmin (2000 pixels). The bleeding and halo

artefacts previously mentioned for g -band, are also present in the rest of the filters. The next observable artefact is the ghost, produced by internal reflections in the HSC and only present in the outer stack of the i , Z , and Y filters. Due to the multiple paths of reflections, ghost features can have different angular sizes. In the Z -band we can clearly see three ghosts: the inner one at a radial distance of $R \sim 170$ arcsec, the middle one at $R \sim 270$ arcsec, and the outermost ghost one located at $R \sim 330$ arcsec. The channel-stop or vertical feature caused by a diffraction pattern in the CCD at long wavelengths ($\sim 1\mu\text{m}$) is only present in the Y -band, where the spikes in the fifth panel of Fig. A2 correspond to the channel-stop higher flux values. In the Y -band, all the stacks (outer, middle, inner, and core) are affected by this feature.

We finally show the 1-D radial profiles of all the HSC-SSP PDR3 in Fig. A3, where each color represents one filter. There is a pair of horizontal and vertical dashed lines matched to each band, where the horizontal one indicates the maximum flux value of the PSF divided by two ($f_{\max}/2$), and the vertical line indicates the FWHM of the PSF also divided by two. By making an approximation across the five bands, the mean FWHM of the HSC-SSP PDR3 PSFs is 0.772 arcsec (~ 4 pixels).

This paper has been typeset from a $\text{\TeX}/\text{\LaTeX}$ file prepared by the author.

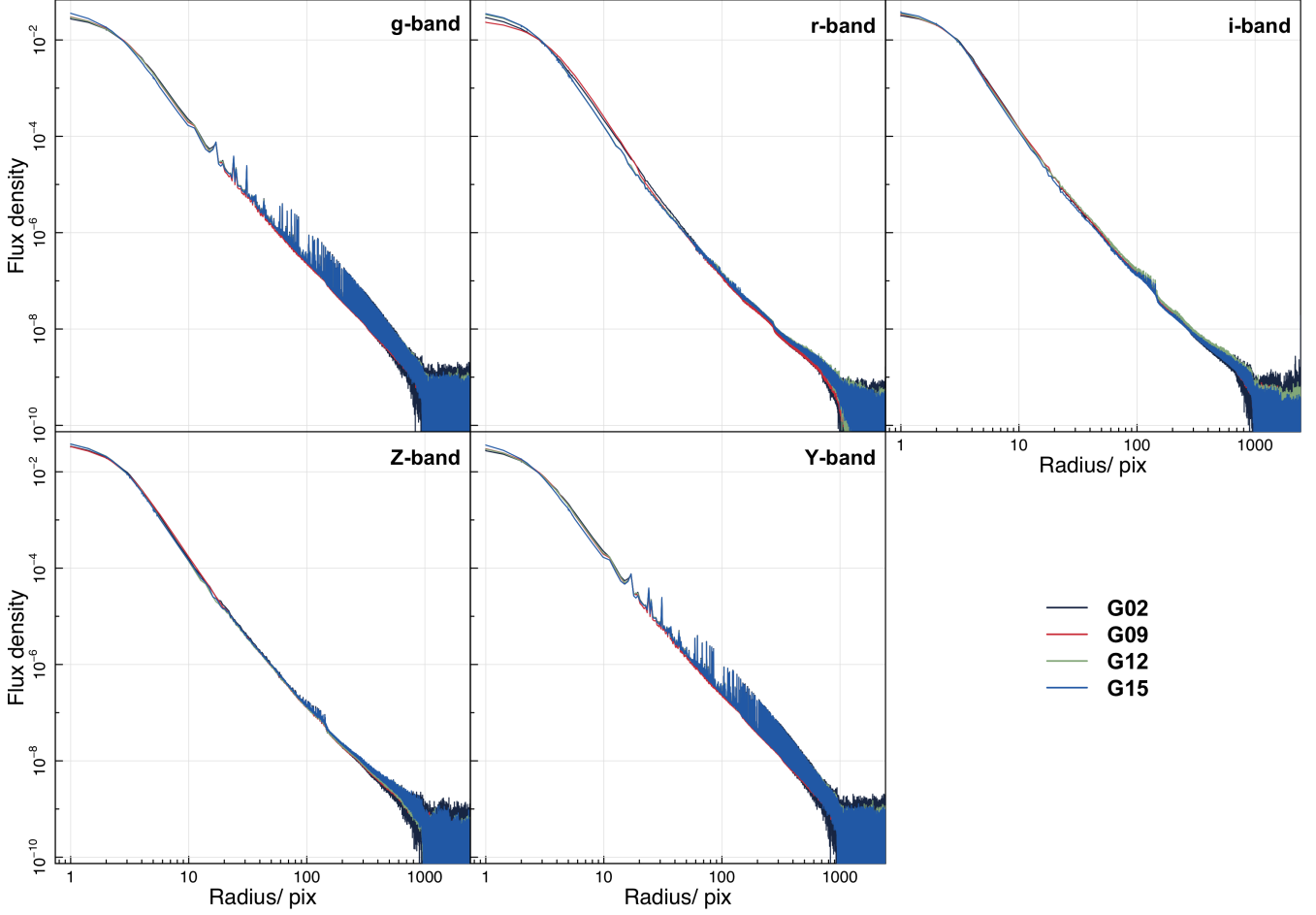


Figure A1. 1-D radial profiles of the HSC-SSP PDR3 PSFs, where each panel corresponds to one HSC filter and the different line colours correspond to the different GAMA regions.

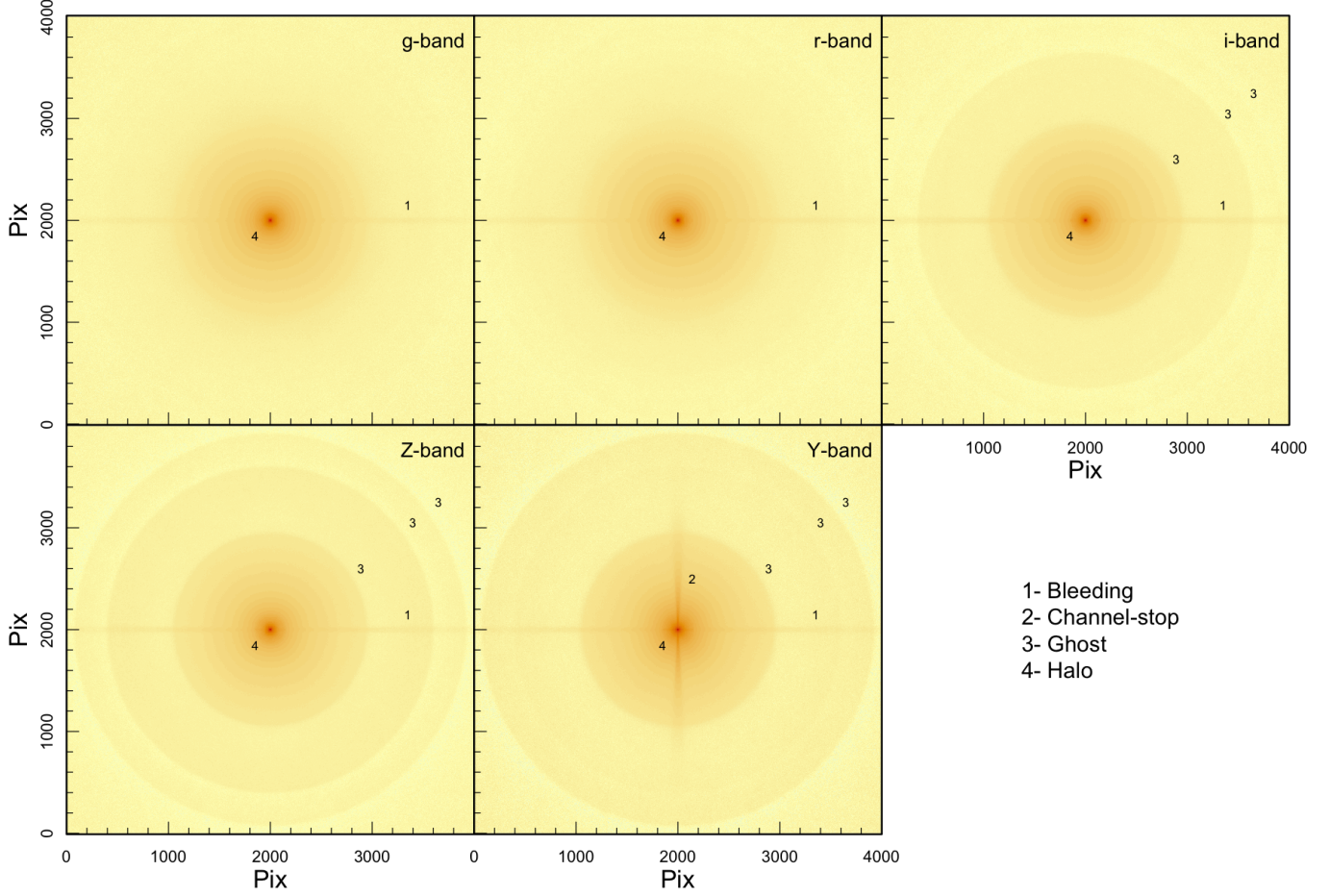


Figure A2. HSC-SSP PDR3 PSFs in the g,r,i,Z and Y filters up to an extent of $R \sim 5.6$ arcmin (2000 pixels), where the optical and detector artefacts are being pointed in each panel. Bleeding (1) is the horizontal feature present in all the HSC filters, channel-stop (2) is the vertical feature (perpendicular to the bleeding direction) only present in the Y -band, the edges of the ghosts features (3) are located at $R \sim 170$ arcsec, $R \sim 270$ arcsec, and $R \sim 330$ arcsec in the i,Z,Y -bands and the smooth halo feature (4) is around the centre of each PSF up to an extent of $R \sim 150$ arcsec.

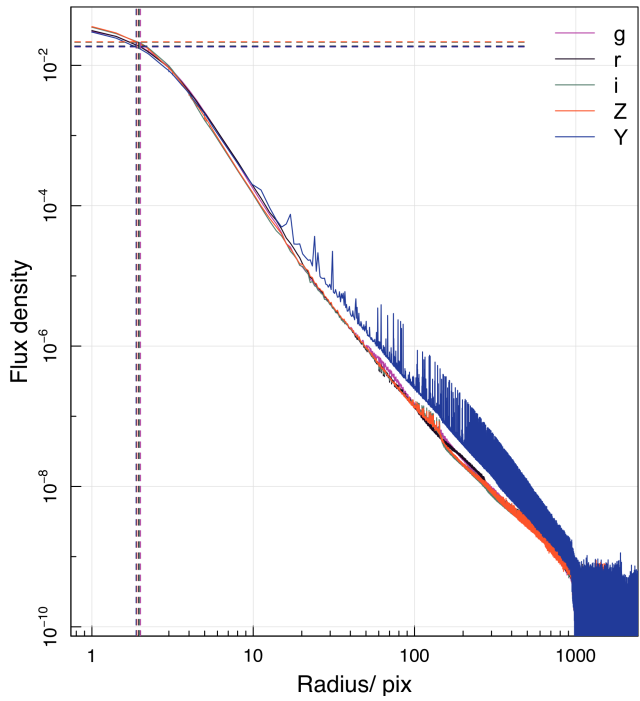


Figure A3. Radial HSC-SSP PDR3 PSF profiles in the five bands. The average FWHM is approximately 0.772 arcsec.